2 (mix)

Lockheed

HUNTSVILLE RESEARCH & ENGINEERING CENTER

LOCKHEED MISSILES & SPACE COMPANY, INC.
A SUBSIDIARY OF LOCKHEED AIRCRAFT CORPORATION

HUNTSVILLE, ALABAMA

LOCKHEED MISSILES & SPACE COMPANY, INC.

HUNTSVILLE RESEARCH & ENGINEERING CENTER

HUNTSVILLE RESEARCH PARK

4800 BRADFORD DRIVE, HUNTSVILLE, ALABAMA

STUDY OF HIGH ALTITUDE
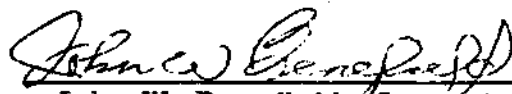## PLUME IMPINGEMENT

FINAL REPORT

January 1973

Contract NAS8-28057
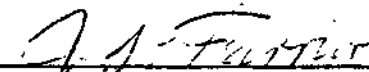
by

J.V. McAnally
S.D. Smith

APPROVED:

John W. Benefield, Supervisor
Fluid Mechanics Section

J.S. Farrior
Resident Director

PRECEDING PAGE BLANK NOT FILMED

FOREWORD

This document presents the results of work performed by the Fluid Mechanics and Thermal Environment sections of the Lockheed-Huntsville Research & Engineering Center. This work was carried out under Contract NAS8-28057, "Study of High Altitude Plume Impingement," for the Aero-Astrodynamics Laboratory of Marshall Space Flight Center. The NASA Contracting Officer's Representatives for this contract were Dr. T.F. Greenwood and Mr. D.C. Seymour.

SUMMARY

A procedure is given for determining the radiation intensities in the base region of the space shuttle vehicle due to solid particle radiation emanating from the solid rocket motors of the shuttle. Results of an analysis of the Titan III and simulated solid rocket motor radiation intensities are presented. A description of the gas particle flow fields of the Titan III nozzle and plume and a space shuttle solid rocket motor nozzle and plume is presented. A discussion of the gaseous Titan III flow fields is presented which utilizes the results of flow fields generated by a gaseous and two-phase method-of-characteristics computer programs. The development of a two-phase computer flowfield analysis program is discussed. An outflow correction theory is developed which will be used to modify existing convection heat transfer methods for better heat transfer predictions on bodies immersed in rocket exhaust plumes.

CONTENTS

Section 1
INTRODUCTION

Successful design of the space shuttle vehicle will depend heavily upon the thermal environment produced by the exhaust of liquid and solid rocket motors which will be used for propulsion, attitude control and separation. The resultant thermal environment due to the rocket exhaust may be caused by heating due to radiation from the plumes and/or direct plume impingement. Reliable analytic models must be available which will predict the environments in the exhaust plumes which contribute to the thermal environment encountered by the shuttle.

The existing techniques for prediction plume impingement heating and radiation heating for liquid rocket motors have shown to be adequate during the Saturn program. However, solid rocket motors complicate the problem of predicting the environment within the exhaust plume. Solid rocket motors have metal additives in the propellant to increase the energy content of the system. These metal additives produce condensed solid and liquid particles in the exhaust gases which radically change the temperatures and pressures which are encountered within the plumes. Therefore, the techniques which were used to predict the plumes of liquid rocket engines must be revised and extended to handle the problems associated with solid propellant motors.

Lockheed-Huntsville has reinitiated work on an equilibrium chemistry coupled two-phase flowfield analysis program under this contract. When this computer program is operational it will be able to describe the exhaust flow field of solid motors as well as existing liquid analyses describe the flow fields of liquid rocket motors. Section 2 of this report briefly describes this computer program and lists its present capabilities. Ultimately the output from this program will be used for determining the environments produced due to plume impingement, solid particle radiation and gaseous radiation.

Section 3 presents the state-of-the-art techniques for predicting the thermal environment encountered by vehicles due to radiation from the solid and liquid particles which are present within a solid rocket motor plume. Because numerous vehicles in the past have been destroyed or severly damaged by this type of heating it is important that the analytic techniques for predicting this type of heating be well understood. Section 3 also presents analysis and comparisons of the results of solid particle radiation studies performed for the Titan III and a simulated space shuttle solid rocket motor.

When undertaking a study to advance the techniques in a field it is of interest to know what the differences in the results are between the old and new techniques. Section 4 presents the results of a study which predicts the exit plane properties of the Titan III 120-inch solid motor utilizing both solid and liquid rocket nozzle analysis programs.

Of further interest of work performed during this contract are methods that were developed for improving the heating prediction techniques of the Lockheed-Huntsville Plume Impingement Computer Program (Ref. 1-1) developed under Contracts NAS8-25511 and NAS8-21463. Current theories for predicting heat transfer rates on vehicles subjected to rocket exhaust impingement do not utilize an adequate theory for predicting corrections which account for the outflow-induced thinning of the boundary layer. Section 5 presents an outflow correction theory that will be used at a future date to modify the existing convective heat transfer methods in the Plume Impingement program.

Section 2
SUPERSONIC TWO-PHASE COMPUTER PROGRAM DEVELOPMENT

The present concept of the space shuttle vehicle has numerous solid rocket motors for main propulsion, separation and abort capabilities. Metal additives are incorporated into the solid propellants of these motors to increase the energy content of the system and also suppress combustion pressure instabilities. The presence of these metal additives results in condensed products in the exhaust gases which can result in several disadvantages. Since the condensed products can do no expansion work, their presence can only detract from the effectiveness of the nozzle to do expansion work in converting thermal to kinetic energy. Also, the presence of liquid or solid particles in the exhaust will contribute significant portions of radiation and plume impingement heating on any structures which are either immersed or in close proximity to the exhaust plume. It is therefore important to know the physical properties throughout the nozzle and exhaust plumes.

An extensive literature survey was made to determine what computer programs were available for calculating two-phase flow fields for use in the space shuttle base heating and plume impingement heating areas. Two basic types of two-phase computer programs were found to exist: (1) uncoupled two-phase programs such as Aeronutronics (Ref. 2-1) and; (2) coupled two-phase programs such as Kliegel's (Ref. 2-2). Uncoupled two-phase programs trace solid or liquid particles through an already generated gaseous flow field and do not consider the effect the particles have on the gas due to drag and heat transfer. Coupled two-phase programs include the effects of the particles on the gas as well as the gas on the particles. However, the existing coupled programs are primarily nozzle performance programs which do not include the flow chemistry (equilibrium or frozen) in the analysis.

2-1

The object of this study was to continue work done under Contract NAS8-21094 (Ref. 2-3), to develop a two-phase computer program which will describe two-dimensional and axisymmetric gas-particle flow fields, including equilibrium and frozen flowfield chemistry and the effect of shock waves. The two-phase capability has been incorporated into Lockheed's Streamline Normal Method-of-Characteristics Computer Program (Ref. 2-4).

The governing equations have been rederived and incorporated into the two-phase streamline normal program. The equations were derived in a form in which the effects of equilibrium chemistry are included. The full development of the equations which will be incorporated into a future document is based on the following assumptions:

- The particles are spherically shaped.
- The total mass of the mixture is constant.
- The total energy of the mixture is constant.
- The particle internal temperature is uniform.
- The gas and particles exchange thermal energy by convection only.
- The gas obeys the perfect gas law and is frozen or in chemical equilibrium.
- The forces acting on the control volume are the pressure of the gas and the drag of the particles.
- The gas is inviscid except for the drag it exerts on the particles.
- There are no particle interactions.
- The volume occupied by the particles is negligible.
- There is no mass exchange between the phases.
- A discrete number of particles, each of different size or chemical species, is chosen to represent the actual continuous particle distribution.
- The particles are inert.

When the final checkout of the two-phase program is completed it will be able to operate in either the two-phase or gaseous-only mode, and the

program will contain the same capabilities as Lockheed's Variable O/F Method-of-Characteristics program described in Ref. 2-5. The two-phase operation of the program will be able to handle up to ten different condensed species with each specie capable of having an input table of specific heat as a function of temperature. The equilibrium or frozen gaseous thermochemistry data will be calculated using a modified version of the NASA-Lewis Chemical Equilibrium Combustion Computer Program (Ref. 2-6). These data will be input to the two-phase program via tape or card input. The output from the two-phase program will contain all the gaseous and condensed species data which are necessary to perform any subsequent radiation heating or plume impingement heating analyses. Upon final checkout of the program a document will be published which contains a complete description of the program as well as a detailed input guide.

Section 3

PARTICLE RADIATION ANALYSIS FOR THE 120-INCH TITAN AND SIMULATED SHUTTLE MOTORS

Design of the thermal protection system (TPS) for the space shuttle will require a thorough knowledge of the heating that results from particle radiation of solid motor exhaust plumes. Excessive heating to the base region has destroyed many of the earlier missiles during liftoff. Because of the weight penalty imposed, excessive insulation for the base region is undesirable. It is therefore extremely important to be able to predict the heating to the base region incurred from the particle radiation. Much of the radiation from solid propellant rocket plumes is due to micron-size alumina particles. The complexity of the problem of predicting particle radiation requires knowledge of the following quantities: (1) particle environment (temperature and pressure distributions of the plume); (2) the size distribution of the alumina particles within the plume; (3) the scattering and absorption coefficients of the particles; (4) the index of refraction of the alumina as a function of temperature and wavelength; and (5) the radiance of the alumina particle cloud.

Numerous methods are available for determining the radiance of a particle cloud from a solid propellant motor but, currently, the most acceptable method is the Chrysler modified version of the Philco-Ford aeronutronics program (Ref. 3-1). This is an uncoupled program in that it considers only particle radiation with no gas radiation calculations performed. The purpose of the current study is to develop a confidence level in the program for future space shuttle studies by using the program to examine the particle radiation effects of two selected solid propellant rocket motors.

The problem of predicting the particle radiation of plumes from solid propellant rocket motors can be divided into two disciplines. These are:

(1) particle environment and trajectory calculations, and (2) particle radiation predictions. Section 3.1 discusses the particle environment and trajectory calculations for the 120-inch Titan motor and a 1.3 scale version of the Titan (which closely approximates the shuttle engine). Relative comparisons are made between the particle trajectories and environments of the two motors. The particle radiation from the two solid propellant rocket exhaust plumes are discussed and compared.

3.1   PARTICLE ENVIRONMENT AND TRAJECTORY

Before particle trajectory or radiation calculations can be performed, a gas flow field must be generated for the nozzle geometry of interest. The gas flow fields for the 120-inch Titan and the approximate shuttle engines were determined using the Lockheed-Huntsville Method-of-Characteristics (MOC) Computer Program (Ref. 2-5) for the supersonic portion of the nozzles. Real gas effects were considered in the flow field and were determined by the Chemical Equilibrium Composition Program (CEC) Ref. 2-6). The Aeronutronics program assumes the gas flow to be ideal and one-dimensional from the rocket chamber to the supersonic section of the rocket nozzle. Problems therefore arose in matching these two theories. A point along the centerline of the nozzle downstream of the nozzle throat, at which there were sufficient characteristics data available, was selected for the interchange of the two theories. The static pressure, static temperature, Mach number and ratio of specific heats (gamma) were determined at this point from the MOC flow field. These local flowfield properties were used with a one-dimensional theory to compute new total conditions in the rocket combustion chamber. With the new total conditions, which were slightly different from the original chamber conditions, and gamma known, a flow field, assuming one-dimension theory, was obtained which matched the MOC flowfield properties at the given point downstream of the nozzle throat. The Aeronutronics program arranges the flowfield, generated by the two theories, by setting up a rectangular mesh

of gas properties at various axial locations from the chamber to the nozzle exit plane and throughout the exhaust plume. This is done in order to provide the necessary environments for the particles in the particle trajectory calculation.

When the gas flow field for the nozzle and plume are completely specified, subroutine TRAJEC, of the Aeronutronics program begins the particle trajectory calculations. The particle trajectory equations are solved by the method of finite difference. As always, the difficulty in using the finite difference method lies in determining the time step such that the stability requirements are met for each of the equations to be solved. The basic equations to be solved by the finite difference method are: (1) particle location (x and y coordinates of the particle); (2) particle velocity; and (3) particle temperature. Reference 3-1 lists these equations along with four equations for determining time steps. The selection of the minimum value of the four time steps calculated should meet the stability requirements in each of the equations. While attempting to determine particle trajectories for the 120-inch Titan it was found that the minimum time step calculated, from the four equations, was so small that the computer run time became excessively long. This minimum time step was to assure stability in the particle temperature calculation. It was decided not to use this time step but instead use the minimum value of the three remaining computed time steps. This was the correct decision in that the run time was greatly reduced with little or no effect on the particle temperature calculations. The only apparent result which could possibly be attributed to an instability in the finite difference equations were very slight temperature oscillations in the combustion chamber. These oscillations soon damped and were completely unnoticed as the particles enter the throat of the nozzle.

Figures 3-1 and 3-2 show the particle trajectories for the 120-inch Titan and shuttle motors, respectively. The particle trajectories for the two motors do not vary much. This is an expected result however, since the shuttle engine and gas flow field are a 1.3 scale version of the 120-inch
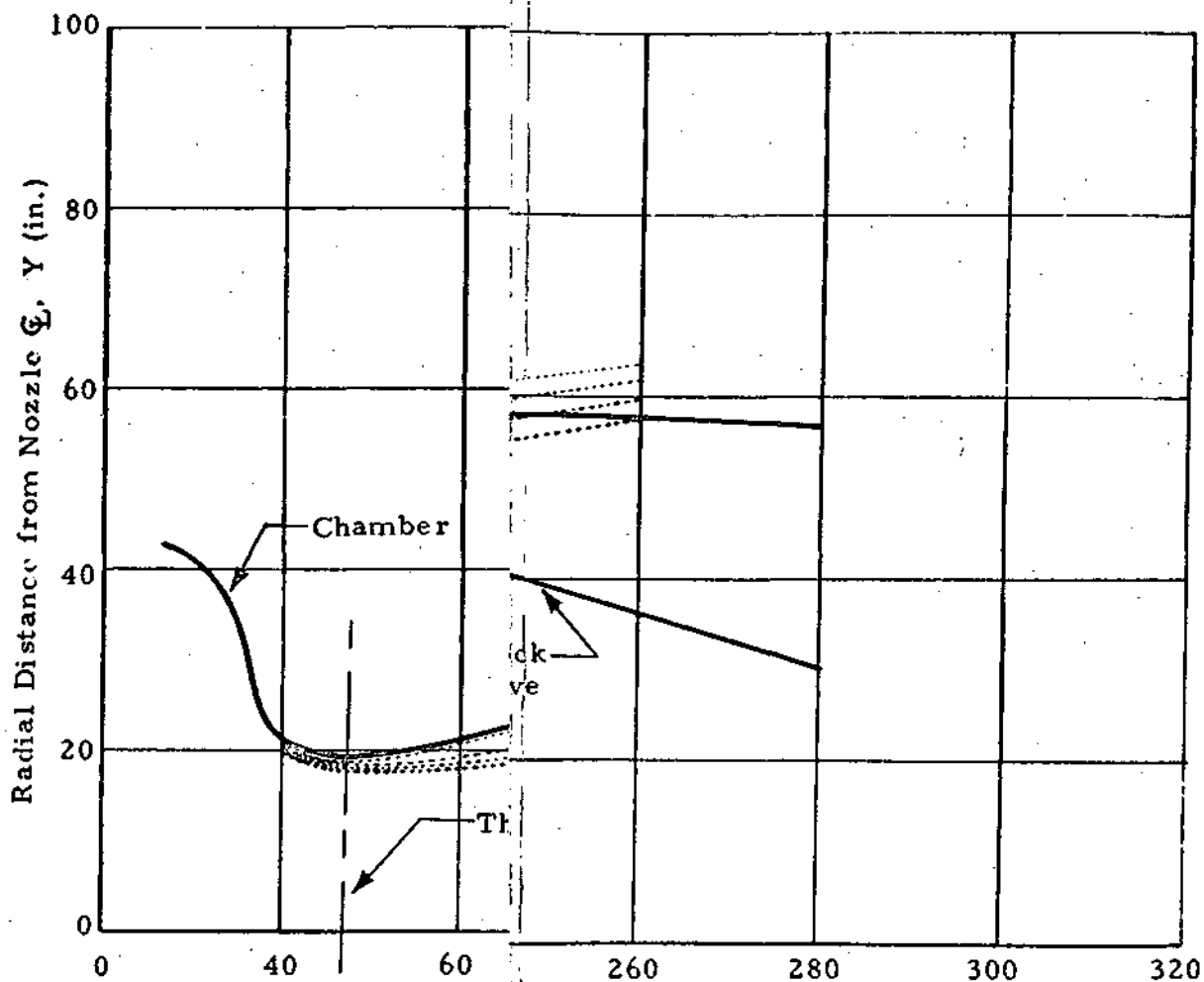
3-3

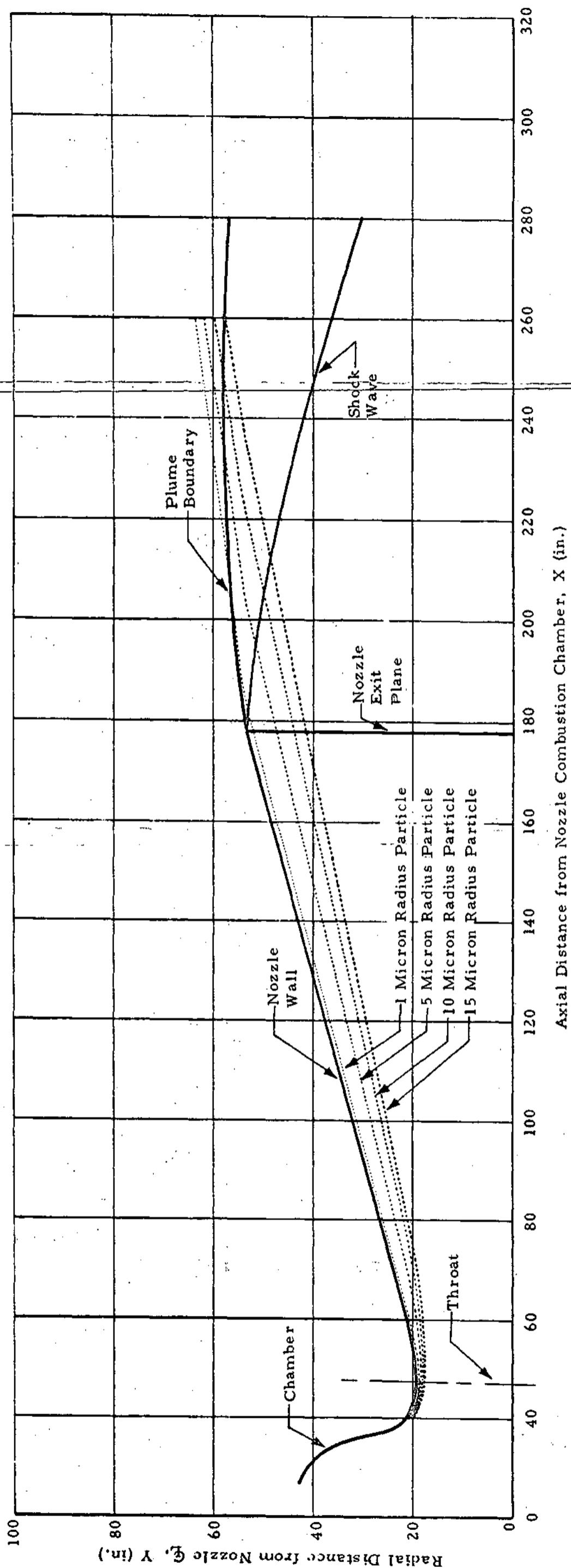Fig. 3-1 - Limiting Particle
Trajectory Plots
for Titan Engine

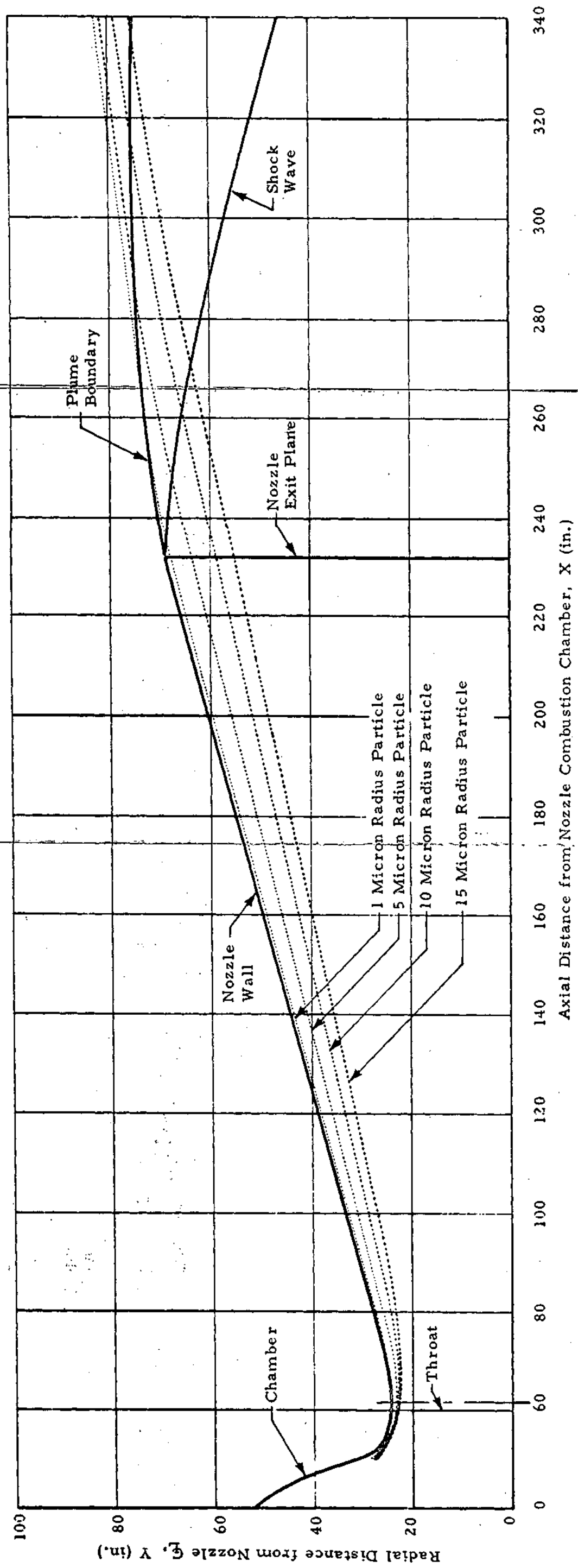Fig. 3-1 - Limiting Particle Trajectory Plots for Titan Engine

Fig. 3-2 - Limiting Particle Trajectory Plots for Shuttle Engine

Titan engine and flow field. The chamber conditions for both engines are essentially the same.

Particle temperature distributions for the Titan and simulated shuttle engines are presented graphically in Figs. 3-3 through 3-6. Figures 3-3 and 3-4 show particle temperatures for centerline trajectories while Figs. 3-5 and 3-6 show particle temperatures for the limiting trajectories. Particle temperature oscillations occurring along the limiting particle trajectories at the nozzle exit plane are evident in Figs. 3-5 and 3-6. There is an increase in the gas temperature due to the plume boundary shock which is attached to the nozzle lip during sea level operation. This leads to a gas temperature that is higher at the plume boundary, immediately downstream from the nozzle exit plane, than any other point in the plume. The gas temperature along this plume boundary remains higher than the temperatures of the plume core until the effects of the boundary shock diminishes. Figure 3-7 is a radial temperature plot for the 120-inch Titan plume. Temperature is plotted versus the non-dimensional parameter, R/R_T, for several X/R_T locations, where R is the radial distance from the plume measured from the chamber and R_T is the nozzle throat radius. The temperature in the plume is essentially constant in the radial direction for each X/R_T location until the flow encounters the boundary shock represented by the discontinuities in the temperature plots. The low thermal capacitance of the smaller diameter particles, which are located on the outermost trajectory closest to the plume boundary, are extremely sensitive to the increased gas temperature. As a result of this sensitivity, the smaller particles experience a sudden increase in temperature. The larger particles, on the other hand, have relatively larger thermal capacitances leading to a considerable time lag for the particles to adjust to the increased gas temperature. This allows the smaller particles to attain higher temperatures than the larger particles. As the effects of the shock wave diminishes downstream of the nozzle exit plane, the smaller particles cool as rapidly as they were heated and once again the larger particles have the higher temperatures.
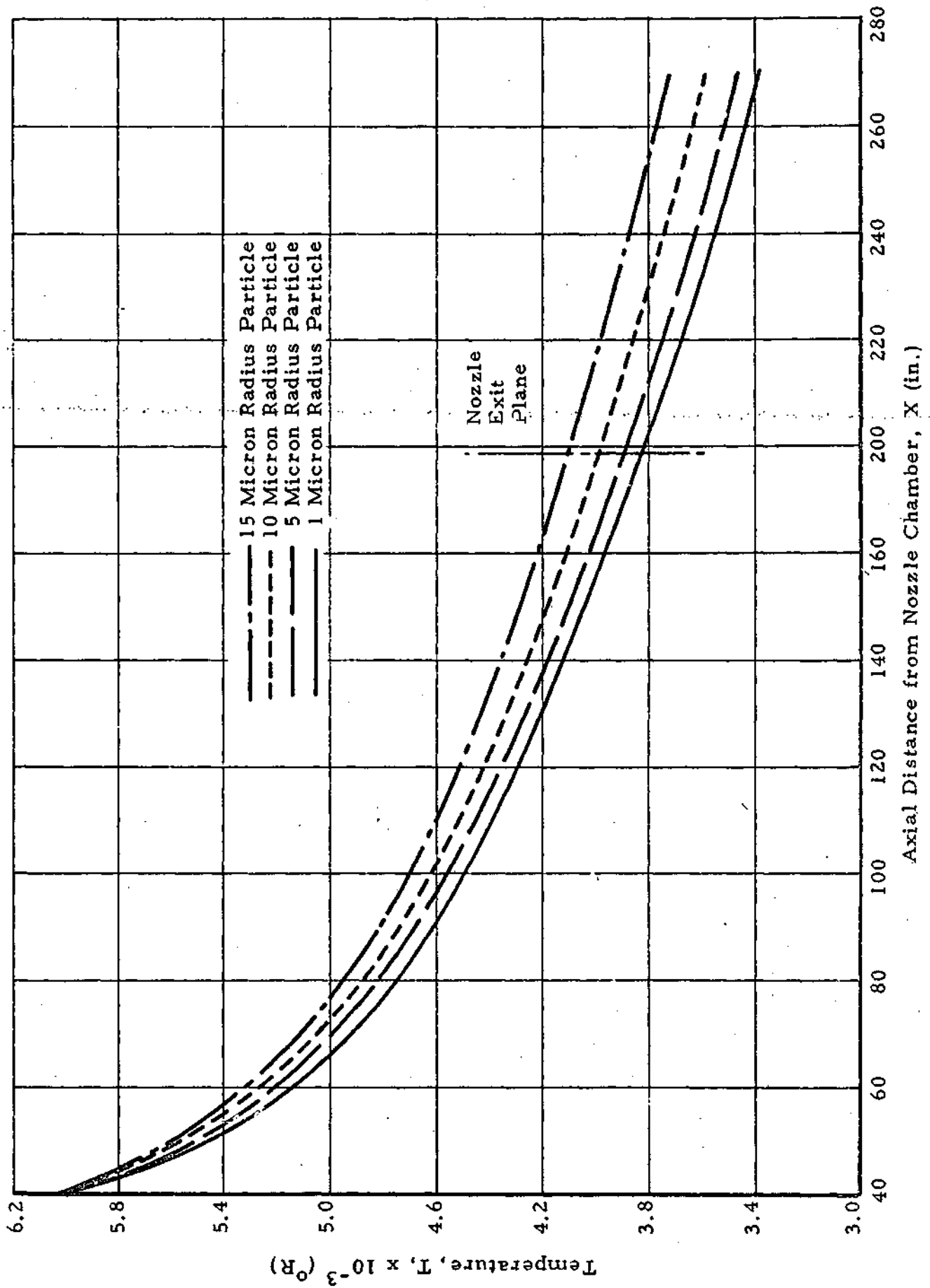
3-6

Fig. 3-3 - Particle Temperature Plot for Centerline Trajectories (120-inch Titan engine)
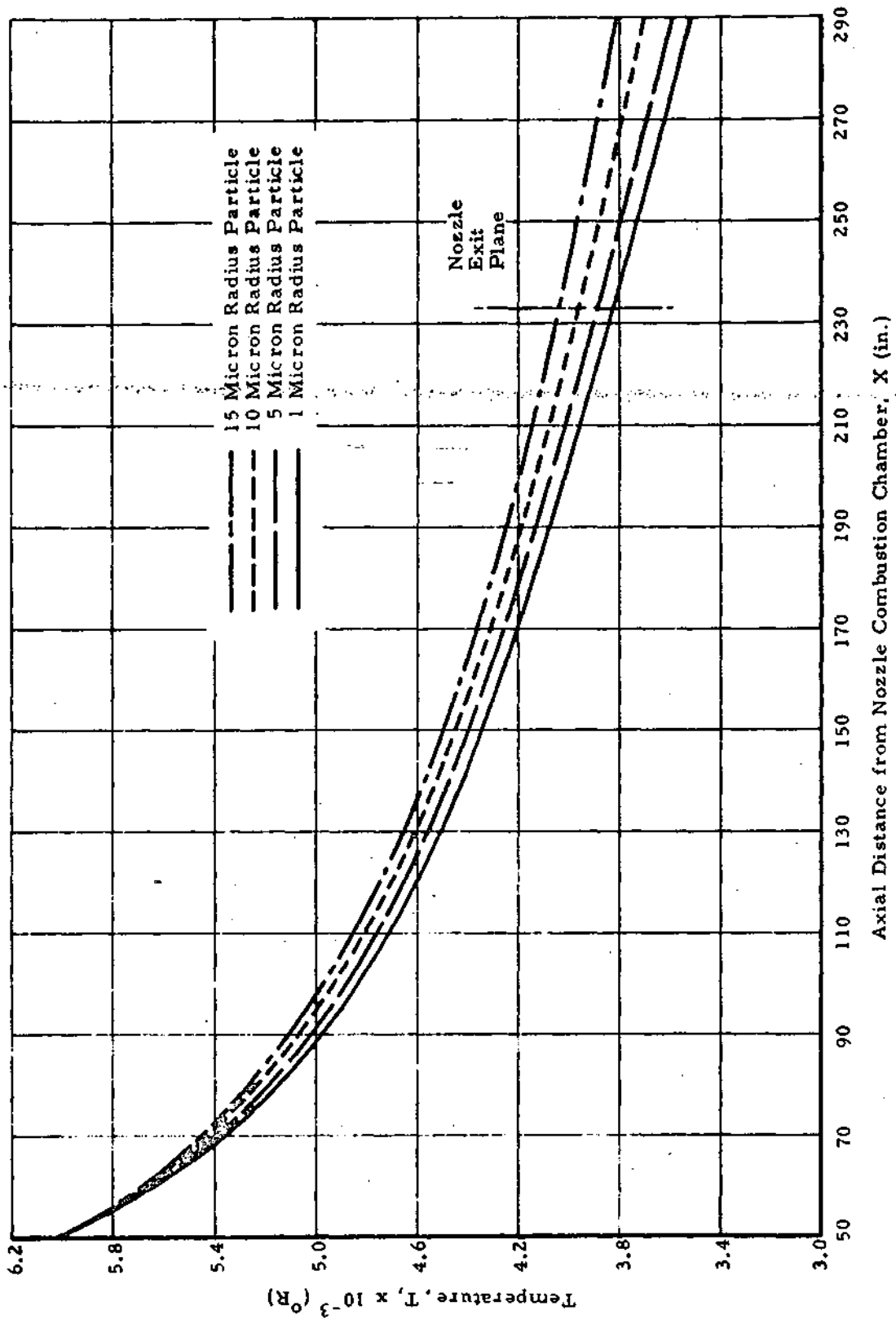
Fig. 3-4 - Particle Temperature Plot for Centerline Trajectories (simulated shuttle engine)
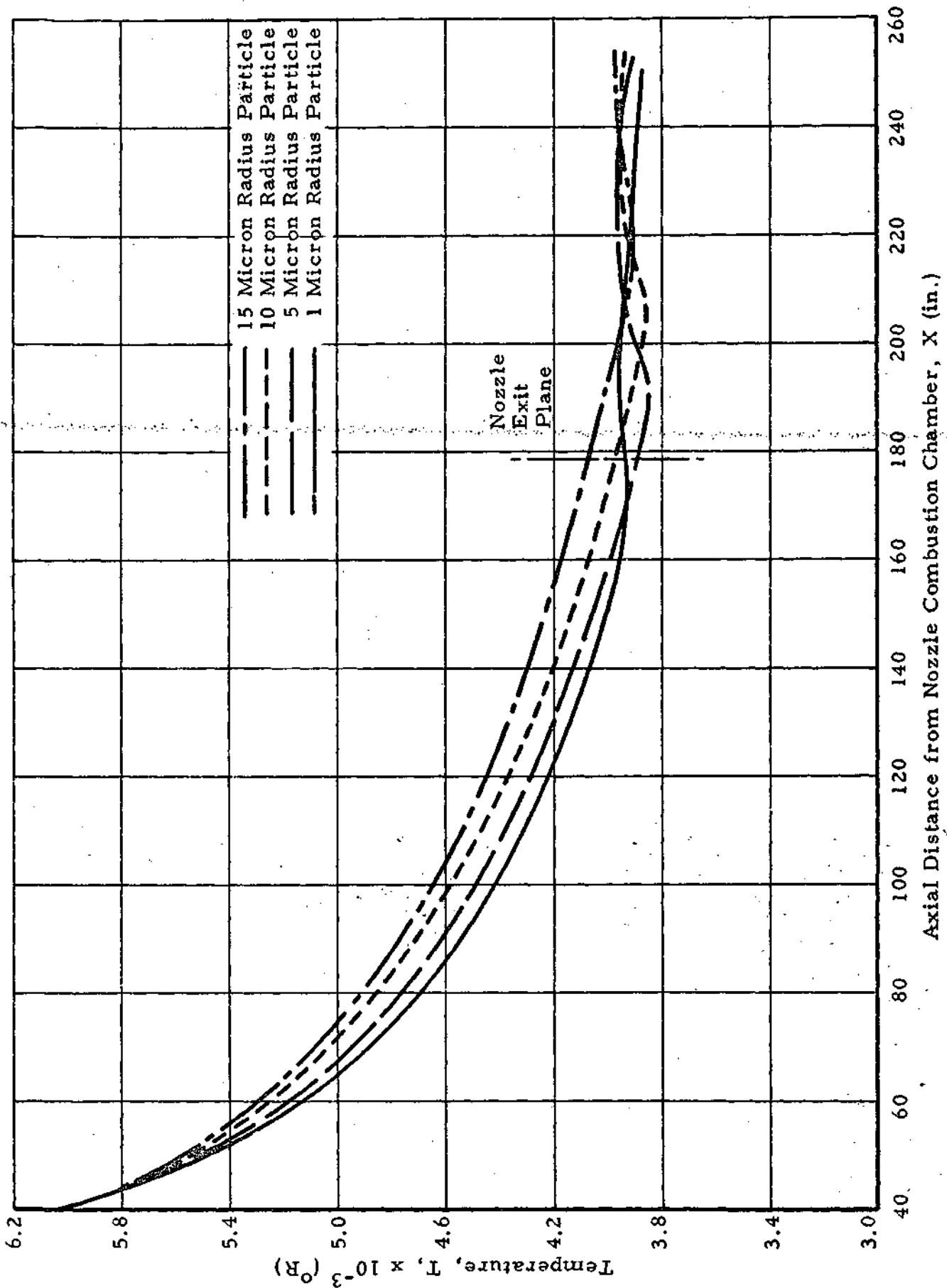
Fig. 3-5 - Particle Temperature Plots for Limiting Trajectories (120-inch Titan engine)
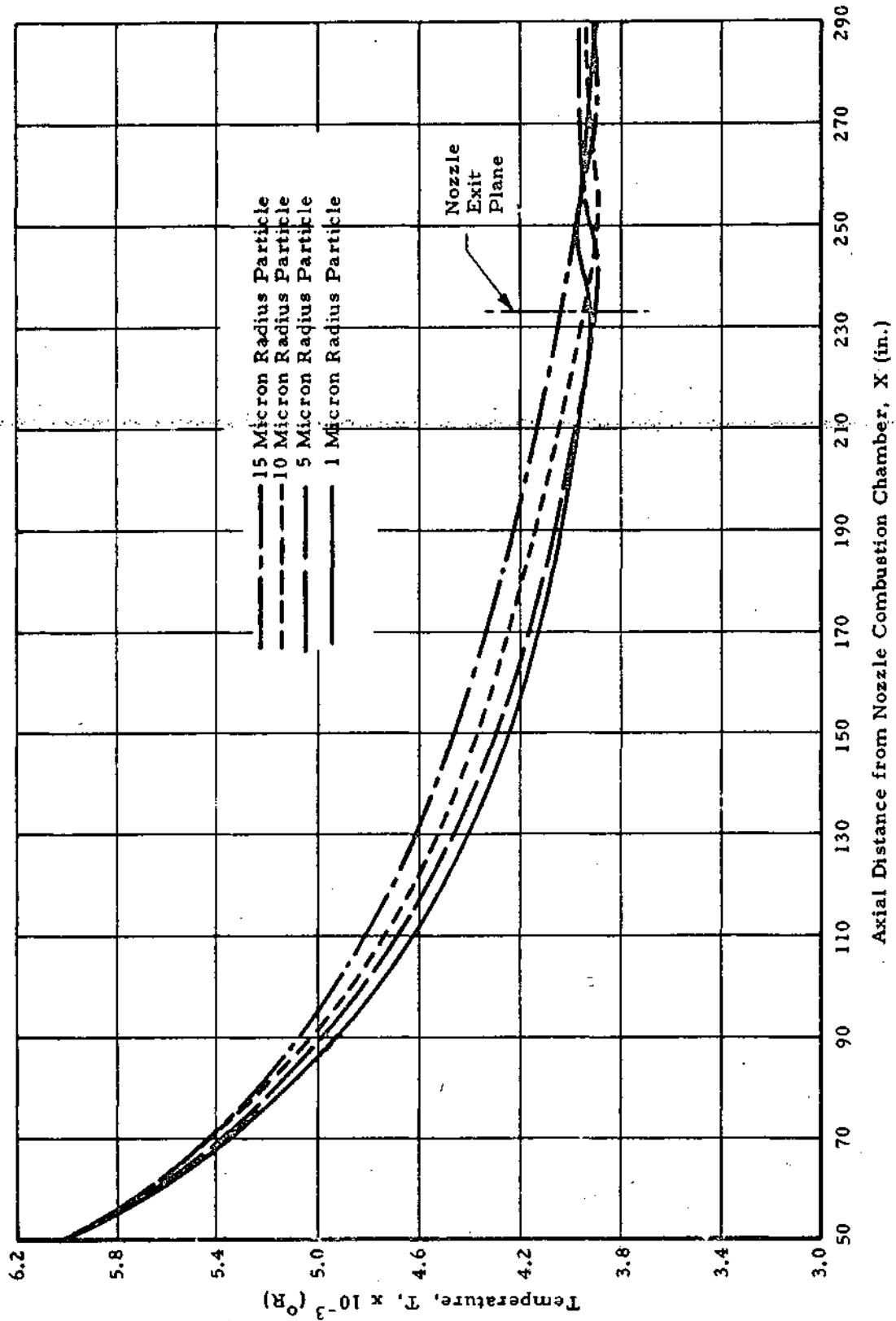
Fig. 3-6 - Particle Temperature Plots for Limiting Trajectories (simulated shuttle engine)
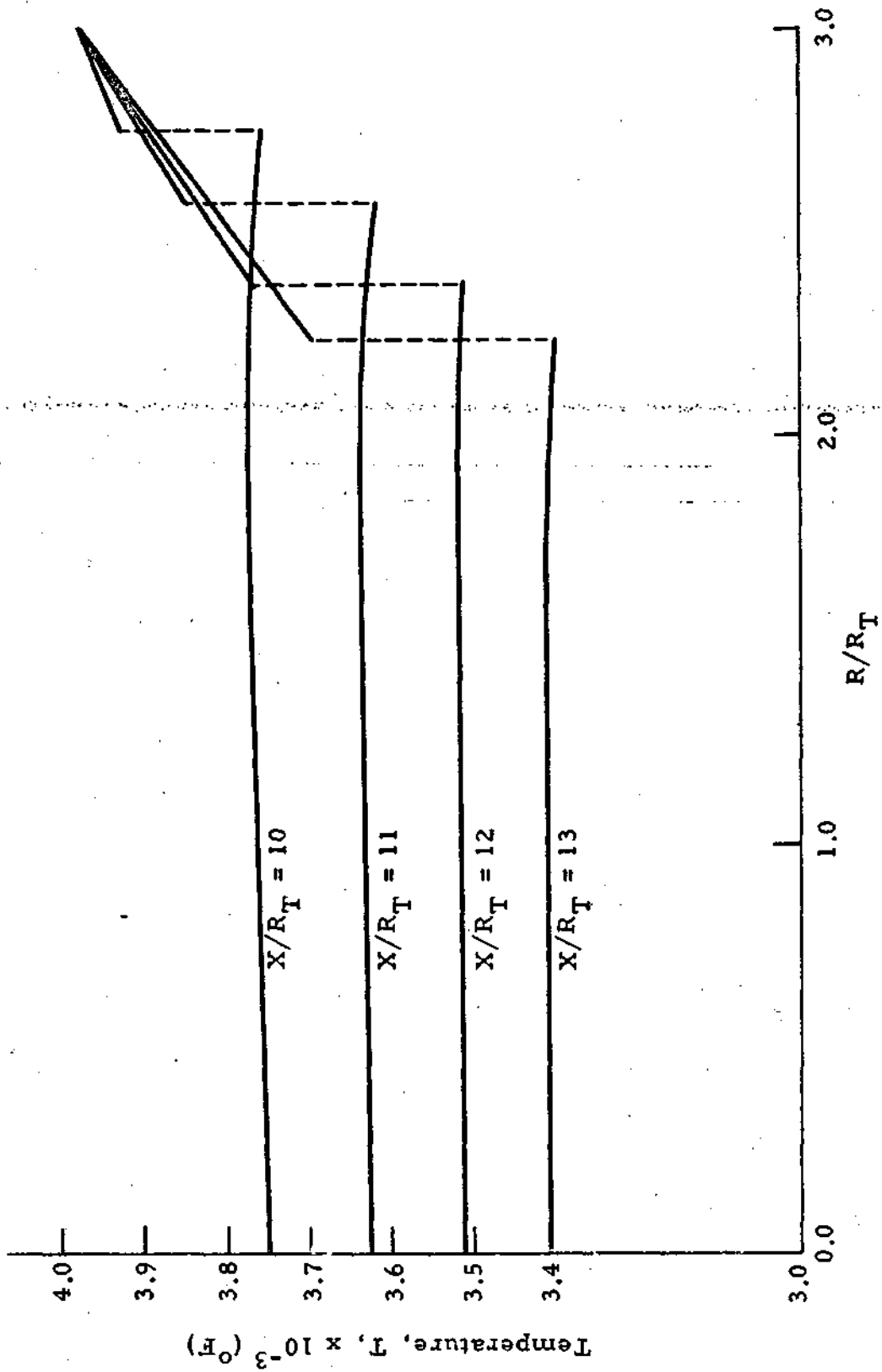
Fig. 3-7 - Radial Temperature Plot for 120-Inch Titan Engine

3.2 PARTICLE RADIATION

The general radiation equation for determining plume radiation heating incident upon a specific target of interest is

$$Q = \int_\lambda \int_\phi \int_\theta I_{\lambda\phi\theta} \sin\theta \cos\theta \, d\theta \, d\phi \, d\lambda \qquad (3.1)$$

At present, the computer program only calculates the spectral intensity, $I_{\lambda\phi\theta}$, emitted by the plume. The triple integration over the two angles, θ and ϕ, and the wave length, λ, is never performed and thus the radiation heat transfer rate Q is not determined. The angles θ and ϕ are input parameters to the program and serve only to orient the line of sight from the plume to the target (see Figs. 3-8 and 3-9).

Particle plume radiation intensity calculations are performed using the Mie scattering theory. The Mie scattering theory considers that the radiation which traverses an inhomogeneous medium such as an optically thin particle cloud is attenuated both by the scattering of the radiation into other directions and by the absorption of radiation by the particles. A digital computer program using the Mie scattering theory is used to determine the backscattering coefficient, β, and the absorption coefficients as functions of particle radius, particle temperature and radiation wave length for the alumina particles in the rocket plume. At a given wave length, the scattering cross sections of a homogeneous spherical particle depend primarily on two parameters: (1) the ratio of particle projected area to radiation wave length, and (2) the index of refraction for the alumina particles. These two parameters must be obtained for input to the Mie scattering program before the scattering, σ_s, and absorption, σ_a, coefficients can be determined. The latter of the two parameters, the complex index of refraction for the alumina particle, is the most difficult to obtain. These values must be determined by experimental means. The output of the Mie program (in the form of σ_a, σ_s, and β as functions of R_p, T_p and λ) has been stored as permanent data for use by the radiation program. The experimental determined index of refractions were determined
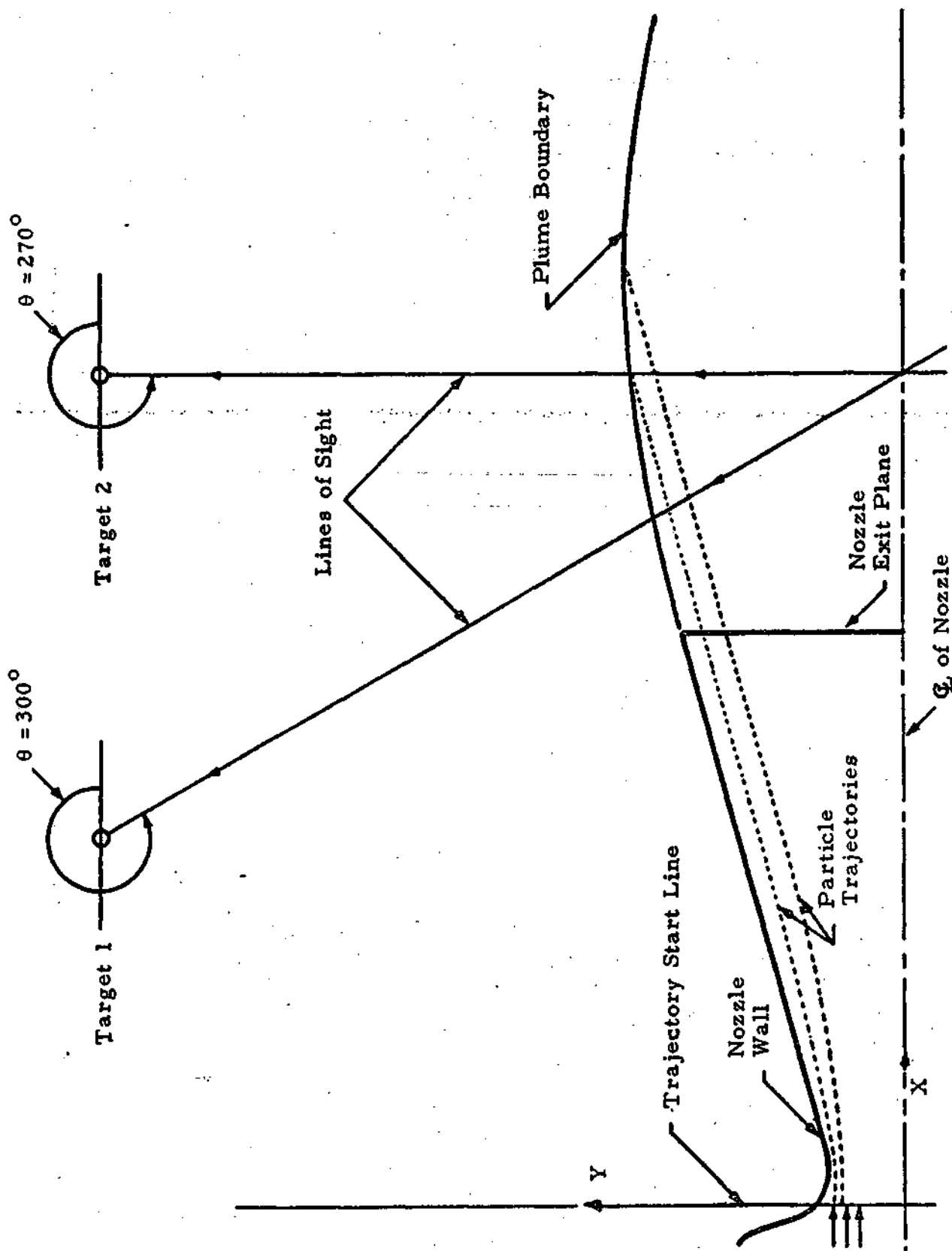
3-12

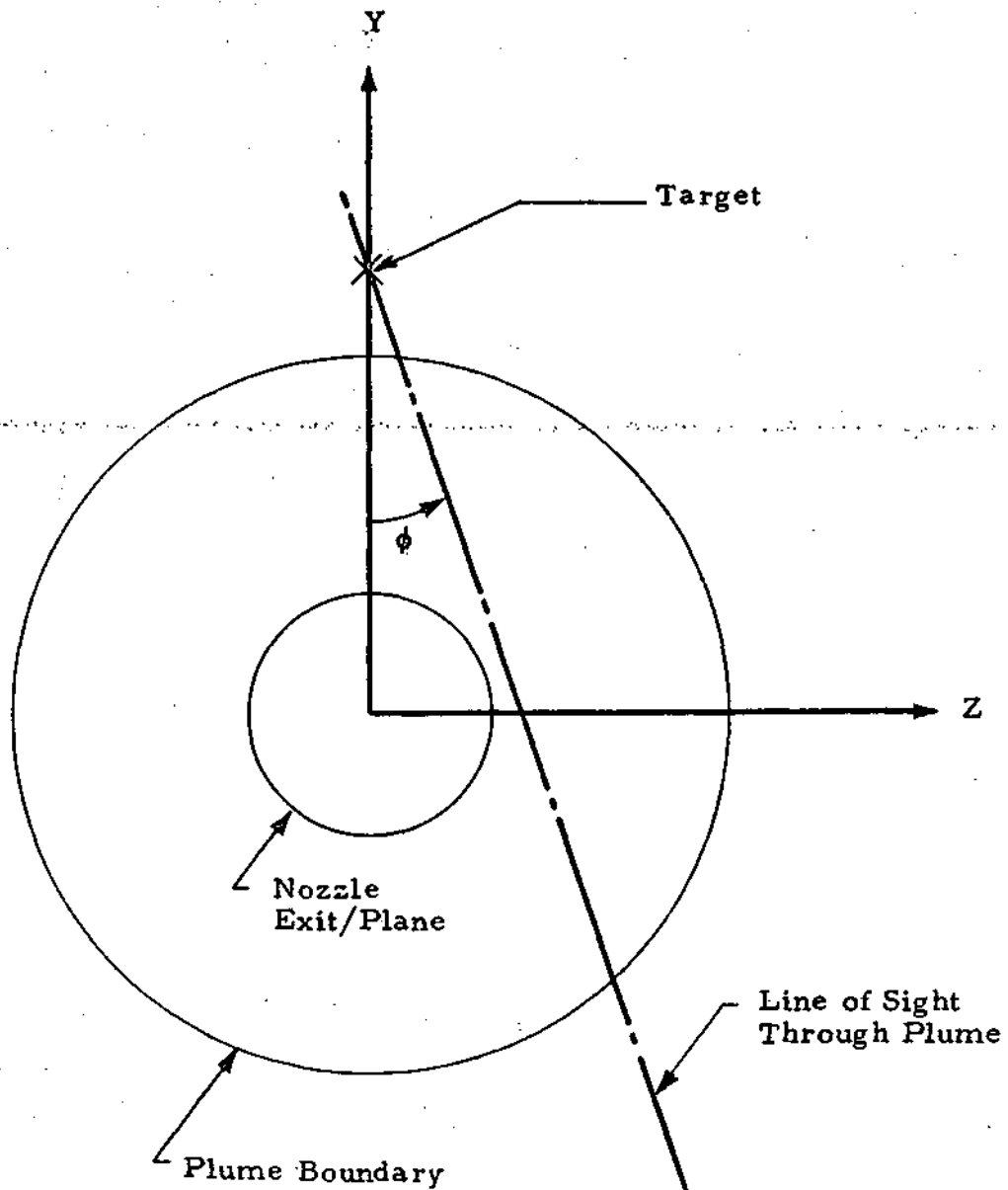Fig. 3-8 - Target Location and Lines-of-Sight Schematic

Fig. 3-9 – Schematic Showing End View of Fig. 3-8

3-14

for wave lengths ranging from 0.5 to 5.0 microns and thus limits the prediction of the absorption and scattering coefficients. Reference 3-1 contains the refractive index for both the molten and solid alumina state.

A variety of different size particles exist at different states in the particle cloud of a two-phase rocket plume. The number distribution of particles in the plume is a function of position because the particle trajectories depend on particle size. The absorption and scattering cross sections are also functions of particle size. Since the particle size is a function of position within the plume the absorption and scattering cross sections are also a function of position.

The particle trajectory program computes the limiting and centerline trajectories and the particle properties along these trajectories for the various particle sizes in the plume. The particle trajectory data are written on magnetic tape for use in the radiation program. Before the data can be used to compute radiation intensity for a specific line of sight through the plume, the trajectory data must be transformed into a more usable form. By performing a linear interpolation axially along each particle trajectory and then between the limiting and centerline trajectories a rectangular mesh of particle properties whose grid size is entirely dependent upon the input value of the print interval, is obtained. The program checks on the line of sight and mesh line intersections to determine particle property variance through the plume. The line of sight through the plume is divided into a number of uniform equally spaced slabs. The number of these slabs is an input parameter. At each interface between successive slabs, along the line of sight, the computer program calculates the number density, particle size distribution, average radiative cross sections and particle energy flux.

Initially, the size distribution in the chamber is given by the skew-symmetric formula

$$\phi[R_p] = \frac{a^{b+1}}{b!}(R_p)^b e^{-aR_p} \qquad (3.2)$$

The size distribution is altered, however, as the particles move downstream by the influence of particle size on diffusion rates. The particle density ratio (the ratio of the local particle density to the chamber density, R_d) is determined for each particle size from the mass continuity relation. The particle density ratio, R_d, corrects the size distribution function, $\phi[R_p]$, as the particles move downstream. At each slab interface the maximum particle radius, R_p max, is determined by surveying the y-coordinates of the limiting trajectories. R_p max is broken down into a number of equal intervals, R_p', such that, R_p', for instance, is equal to R_p max/50. Using R_p' in Eq. (3.2) and multiplying by the initial number of particles per unit volume in the chamber (input parameter RNTC) and the particle density ratio R_d, the total number of particles per unit volume, N_t, present at the particular location is determined by the following integration

$$N_t = \int^{R_p \, max} \left[\phi(R_p')(N_T)(R_d)\right] dR_p \qquad (3.3)$$

The scattering and absorption coefficients previously discussed, are dependent not only on wave length and temperature but also particle radius. The coefficients used in the radiation program at each slab interface are average values. Calculation of the average scattering coefficient, $\overline{\sigma}_s$, is determined from the following equation.

$$\overline{\sigma}_s = \frac{1}{N_t} \int^{R_p \, max} \sigma_s\left[T_p, \lambda, R_p'\right] \cdot N\left[R_p'\right] dR_p \qquad (3.4)$$

where $N(R_p')$ is equal to $\phi(R_p) \cdot N_t \cdot R_d$. The particle radiative properties $\overline{\sigma}_a$ and $\overline{B}$ are averaged over the size distribution that exists at each point along the line of sight as in Eq. (3.4) for $\overline{\sigma}_s$. Once all the radiative properties have been obtained for each slab interface on the particular line of sight through the plume, the radiation intensity equations are solved to determine the net spectral radiation intensity from the plume to the target.

The initial size distribution in the chamber for the Titan is shown in Fig. 3-10. This curve is of the form of Eq. (3.2) where a = 2.0 and b = 1.0. The initial size distribution in the chamber of the shuttle was assumed the same as the size distribution in the 120-inch Titan.

There were two basic target locations for both the 120-inch Titan and shuttle motors investigated in the particle radiation analysis. Figure 3-8 schematically shows two target locations and the corresponding lines of sight. This schematic can be applied to either the 120-inch Titan or shuttle motor since the two targets are in basically the same location for each of the two engines. The two target locations for the 120-inch Titan motor are: (1) X = 129 inches, Y = 180 inches, and (2) X = 209 inches, Y = 180 inches. The two target positions for the shuttle are: (1) X = 167.5 inches, Y = 234 inches, and (2) X = 272 inches, Y = 234 inches. The angles θ_1 and θ_2 are 300 and 270 degrees, respectively, and are the same for the 120-inch Titan and shuttle targets. The two angles (θ_1 and θ_2) along with the angle ϕ (see Fig. 3-9) orient the line of sight from the plume to the target. A radial survey of the plume was performed for each of the lines of sight for the two cases. This was done to determine the effects of varying the angle ϕ on the radiation intensity calculations. Figures 3-11 through 3-14 are radiation intensity versus wave length plots for two targets in question for the 120-inch Titan and shuttle engines. In particular, Figs. 3-11 and 3-12 show intensity as a function of wave length at the target 1 location for the Titan and shuttle engines, respectively. Figures 3-13 and 3-14 are the same basic intensity plots for the 120-inch Titan and shuttle engines determined at the target 2 location.

Upper and lower bounds are placed on the intensity emitted from a particle plume to a specific target. The backscattering coefficient, β, determines these bounds. The maximum radiation intensity emitted by the plume (I_o(max)) incident on a target considers the backscattering coefficient to be zero, i.e., the medium the target sees has maximum emittance and no reflectance. The other extreme, or the minimum radiation intensity emitted by the plume (I_o(min)), considers maximum scattering ($\beta = 1$) i.e., the medium exhibits maximum reflectance. $I_o(\beta)$ is the radiation intensity value using the backscattering coefficient, β, determined by the Mie scattering theory.

$$\phi\left[R_p\right] = \frac{a^{b+1}}{b!}\left(R_p\right)^b e^{-aR_p}$$

Solid Particle Radius, R (microns)
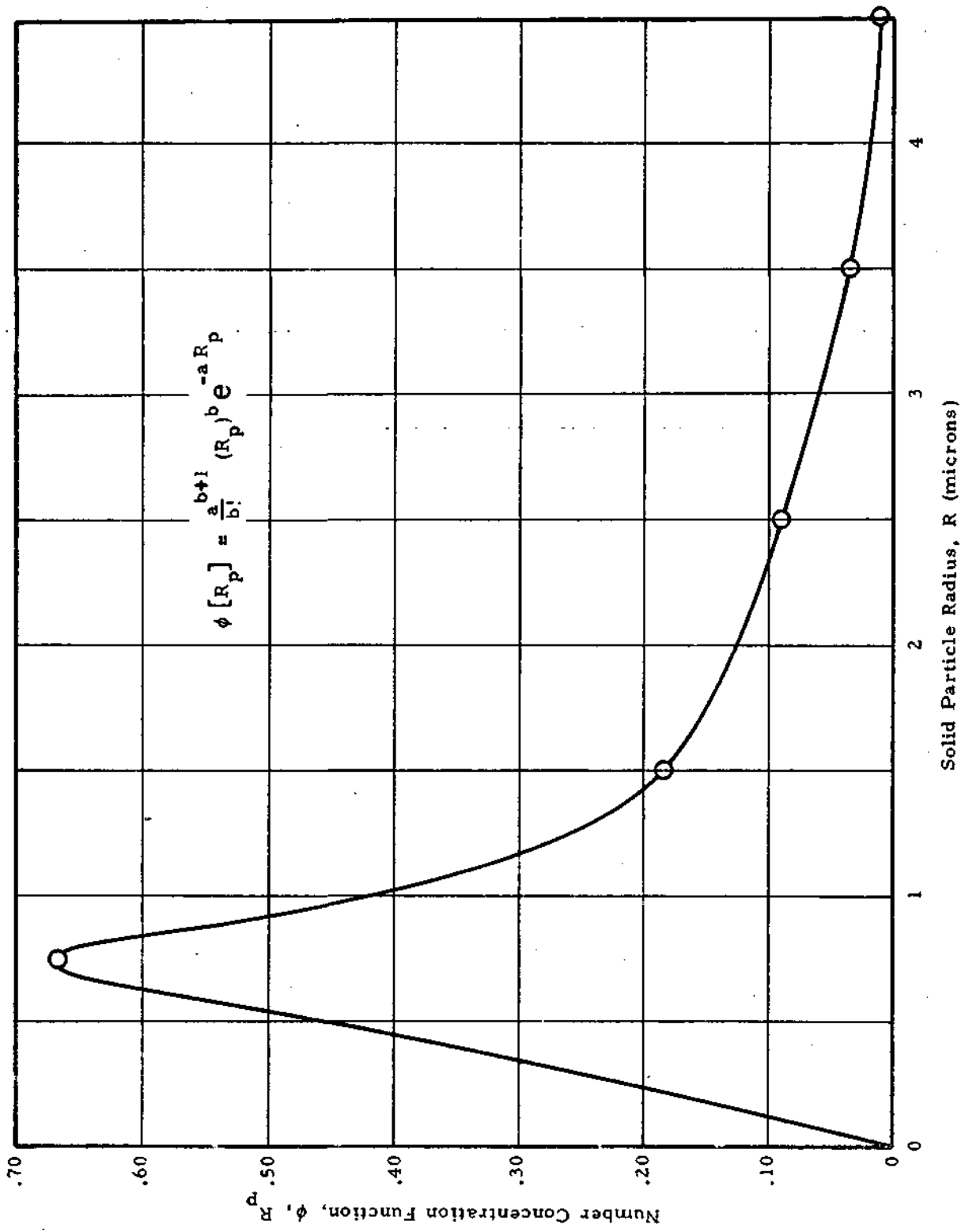
Fig. 3-10 - Initial Chamber Particle Distribution for 120-Inch Titan

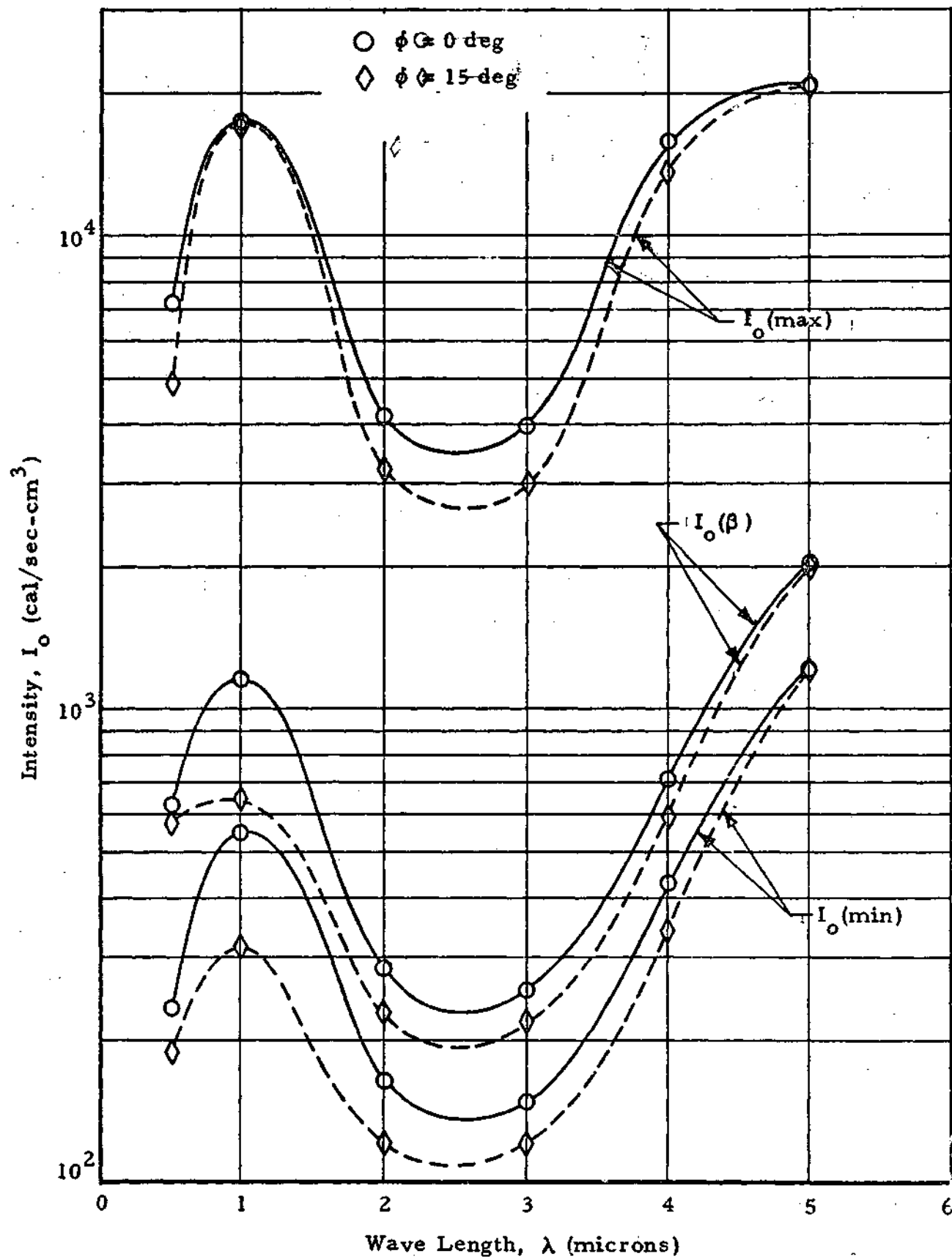Number Concentration Function, ϕ, R_p

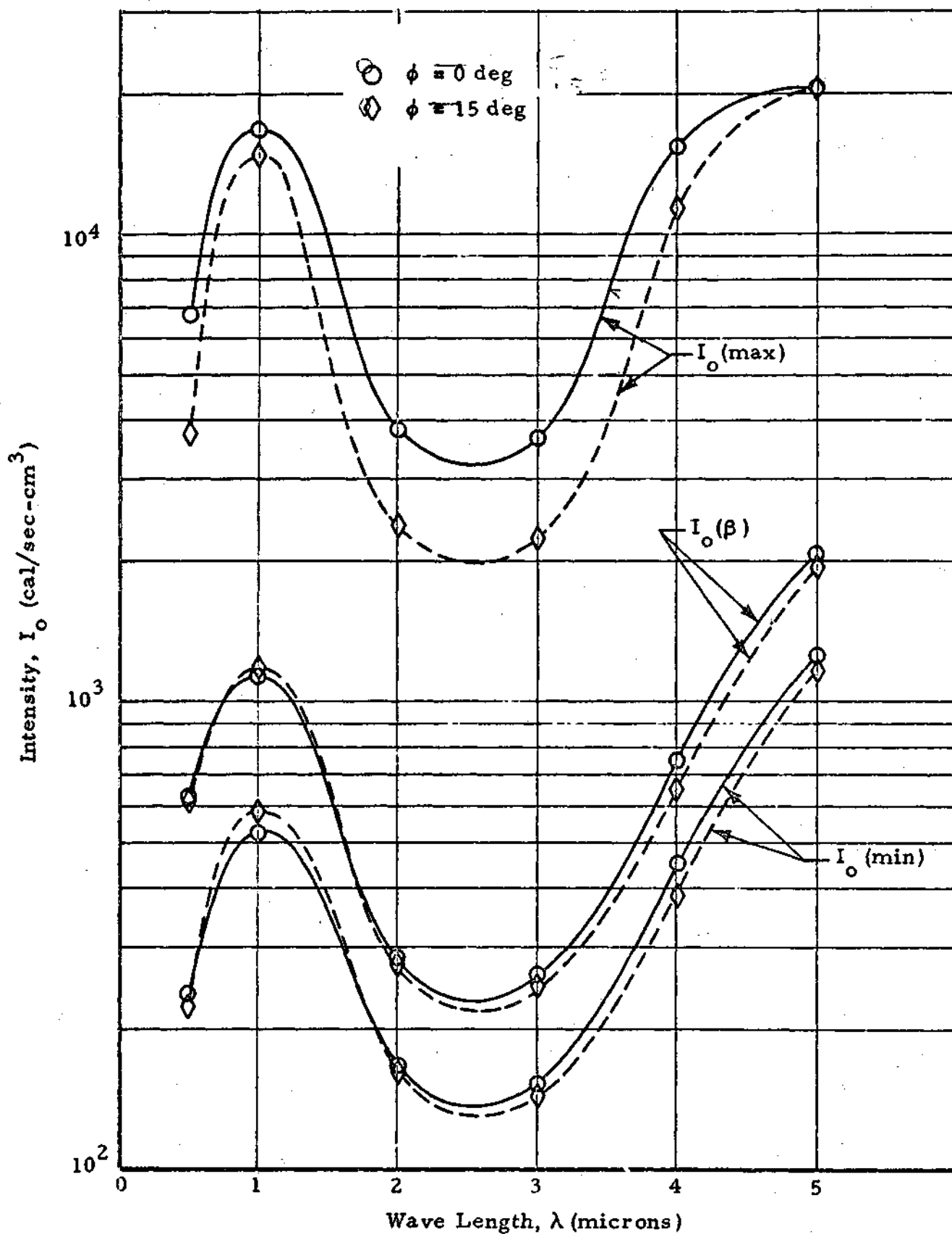Fig. 3-11 - Target 1 Radiation Intensities for Titan

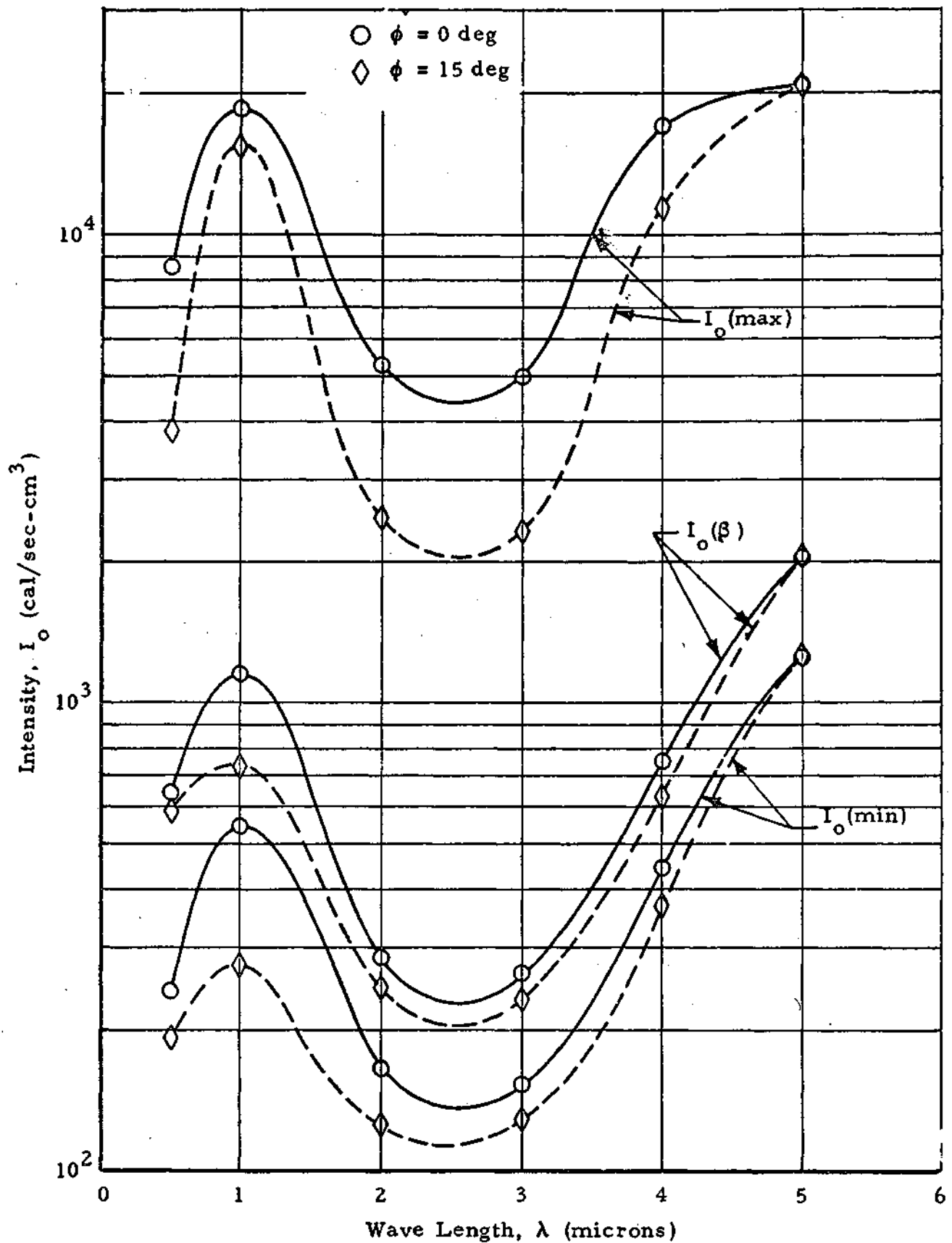Fig. 3-12 - Target 1 Radiation Intensities for Shuttle
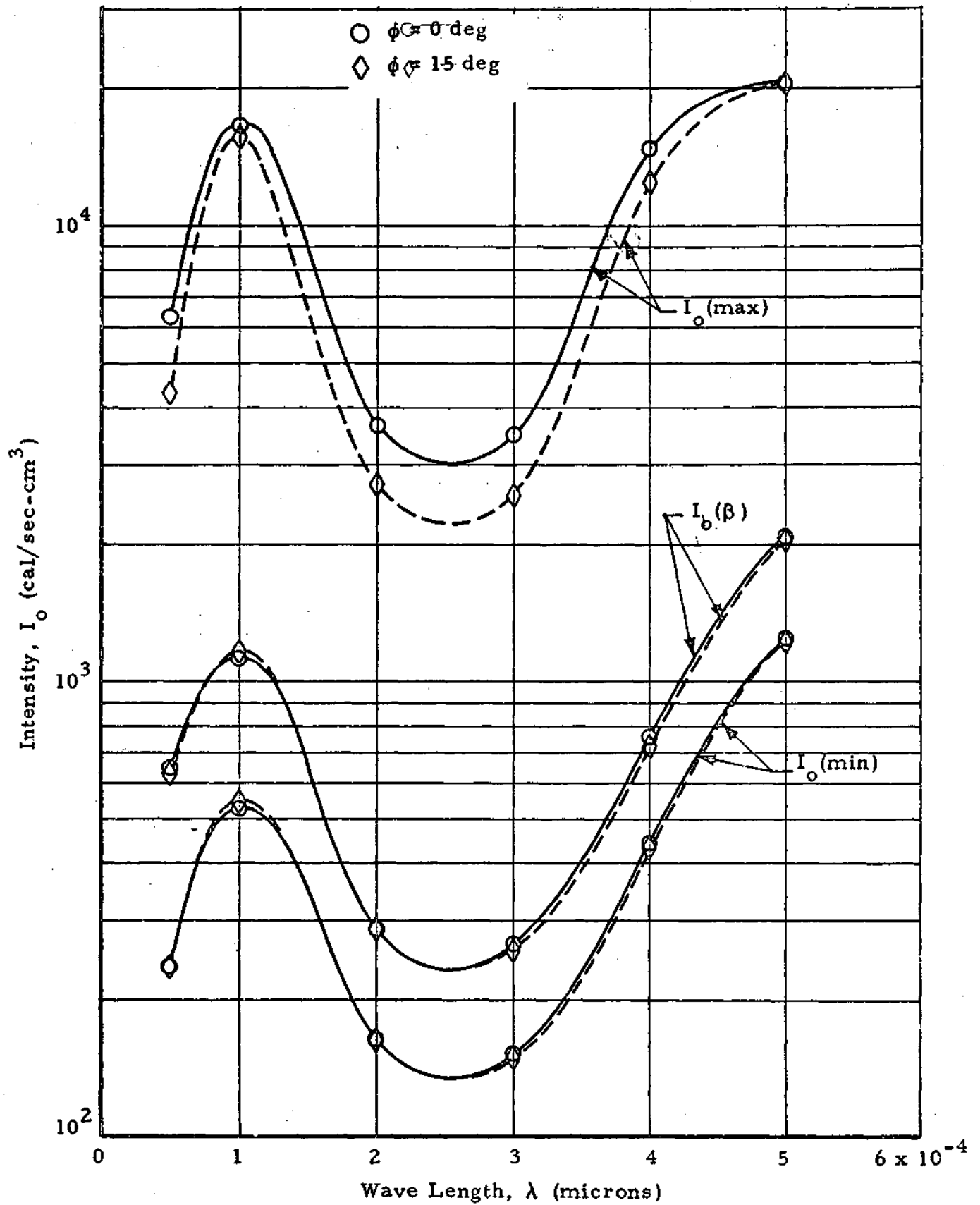
Fig. 3-13 - Target 2 Radiation Intensities for Titan

3-21

Fig. 3-14 - Target 2 Radiation Intensity for Space Shuttle

3=22

For a very thin medium, or a plume containing only a few particles which is usually the case in the small S-IVB ullage and retro motors (Ref. 3-1), the upper and lower bounds are nearly equal, whereas in a more dense plume with many particles the limits become wider. The exhaust plumes of the 120-inch Titan and shuttle motors are very dense with particles due to the high concentration of alumina in the solid propellant for the two engines. The effect of the dense particle plumes are exhibited in the radiation intensity plots shown in Figs. 3-11 through 3-14. Notice the wide spread (approximately two orders of magnitude) between the I_o(max) and I_o(min) plots in each of the figures. This variation indicates the importance of considering the back-scattering effects in the more dense particle plumes. In each of the figures (Figs. 3-11 through 3-14) notice the decrease in the spectral intensity curves at the 2 and 3 micron wave lengths. This decrease is due to the radiation blockage occurring as a result of the mean particle radius being on the same order of magnitude as the wave length.

3.3 PLANK'S QUANTUM ARGUMENTS

It has been shown by the quantum arguments of Planck and verified experimentally that for a black body the spectral distributions of hemispherical emissive power and radiant intensity in a vacuum are given as a function of absolute temperature and wave length by

$$e_{\lambda_b}(\lambda) = \pi i'_{\lambda_b}(\lambda) = \frac{2\pi C_1}{\lambda^5 \left(e^{C_2/\lambda T} - 1\right)} \tag{3.5}$$

where $e_{\lambda_b}(\lambda)$ and $i_{\lambda_b}(\lambda)$ are the emissive power and intensity, respectively, and λ is the wave length, T the absolute temperature and C_1 and C_2 are constants determined by Planck. To better understand the implications of Eq. (3.5), it has been plotted in Fig. 3-15. Here the hemispherical spectral intensity is given as a function of wave length for several different values of the absolute temperature. One characteristic of Fig. 15 that is quite evident is that the intensity emitted at all wave lengths increases as the temperature
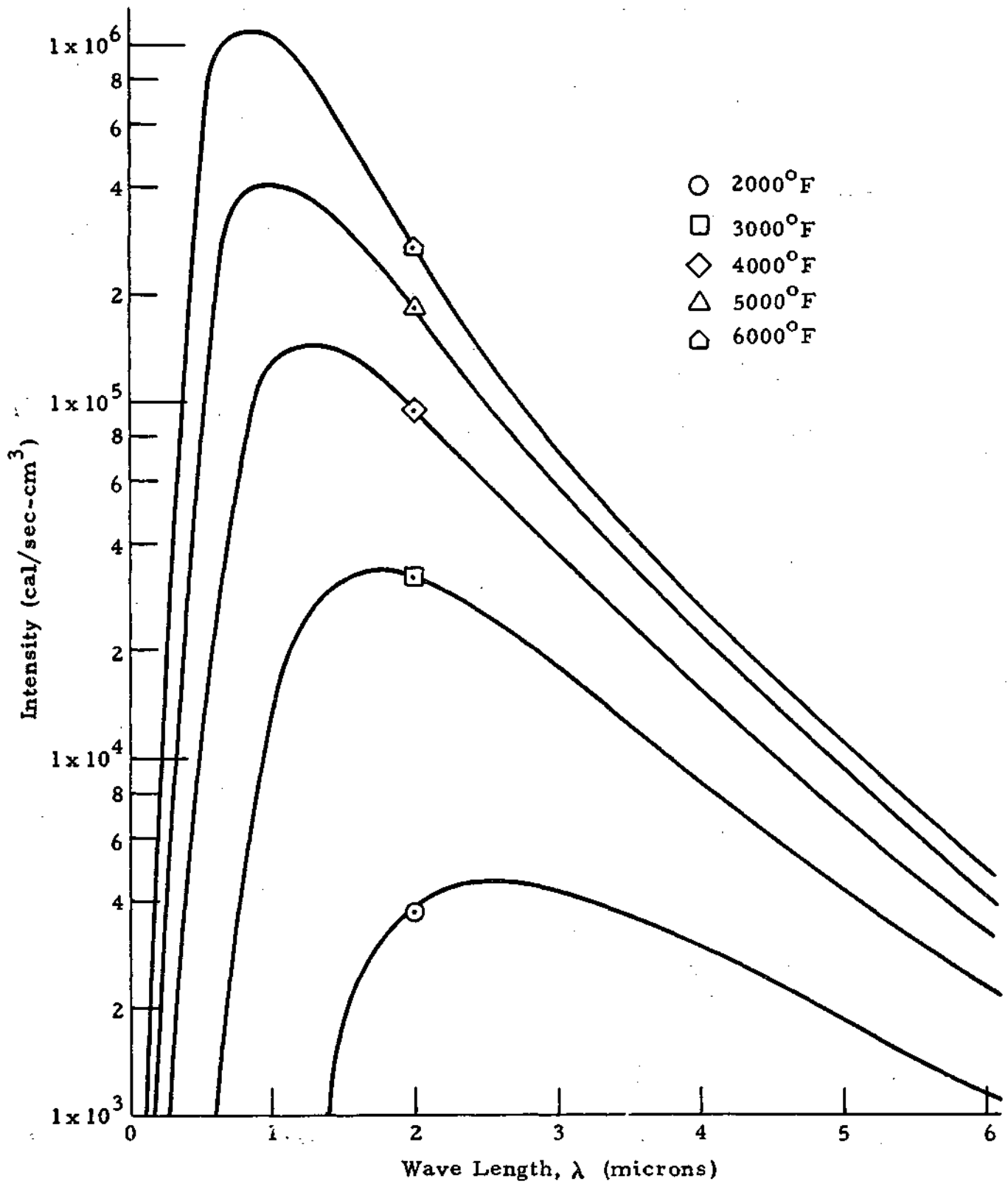
3-23

Fig. 3-15 - Blackbody Radiation Intensity as a Function of Wave Length and Temperature

increases. Another characteristic of Fig. 3-15 is that the peak of the spectral intensity shifts toward the smaller wave length as the temperature increases. The black body is defined as a perfect absorber and is also a perfect emitter. Its spectral intensity and therefore its spectral emissive power are only functions of the temperature of the black body. In each of the figures, there is a sudden increase in the spectral intensity values in the 3.0 to 5.0 micron wave length range. The spectral intensity value I_o(max) at the 5.0 micron wave length is comparable to that intensity emitted by a black body at a temperature between 2000°F and 3000°F (see Fig. 3-15).

3.4   RESULTS

Because the spectral intensity plots for the 120-inch Titan and shuttle motors reveal only slight variations in the spectral intensity values for the two motors, it can be assumed that the radiation heat transfer to the targets of interest is basically the same in each case. While it is true that at present there is no narrow view spectrometer data available for direct comparison with the analytical results, there is sufficient calorimeter data available for the 120-inch Titan motor. These data are presented in Ref. 3-2. Some of the calorimeter locations for the full-scale Titan motor static firings are shown in Fig. 3-15. Figure 3-16 also shows the X, Y, Z coordinates as well as the direction angles for each calorimeter. The radiation heat data was obtained from two 120-inch diameter motor static firings. Table 3-1 shows the results of one of these static firings. The principle targets selected in this analysis were the C012 and C009 targets (see Fig. 3-16). Since the simulated shuttle motor in this analysis is a 1.3-scale version of the 120-inch Titan motor, the Titan target coordinates were scaled by 1.3 to establish the shuttle target coordinates. This was done in order to maintain basically the same relative target positions between the two motors. Since the analysis indicated the same spectral intensity values at the two target positions for each motor, the experimental radiation heat transfer rate determined from the static firings of the 120-inch Titan motor can be assumed the same.
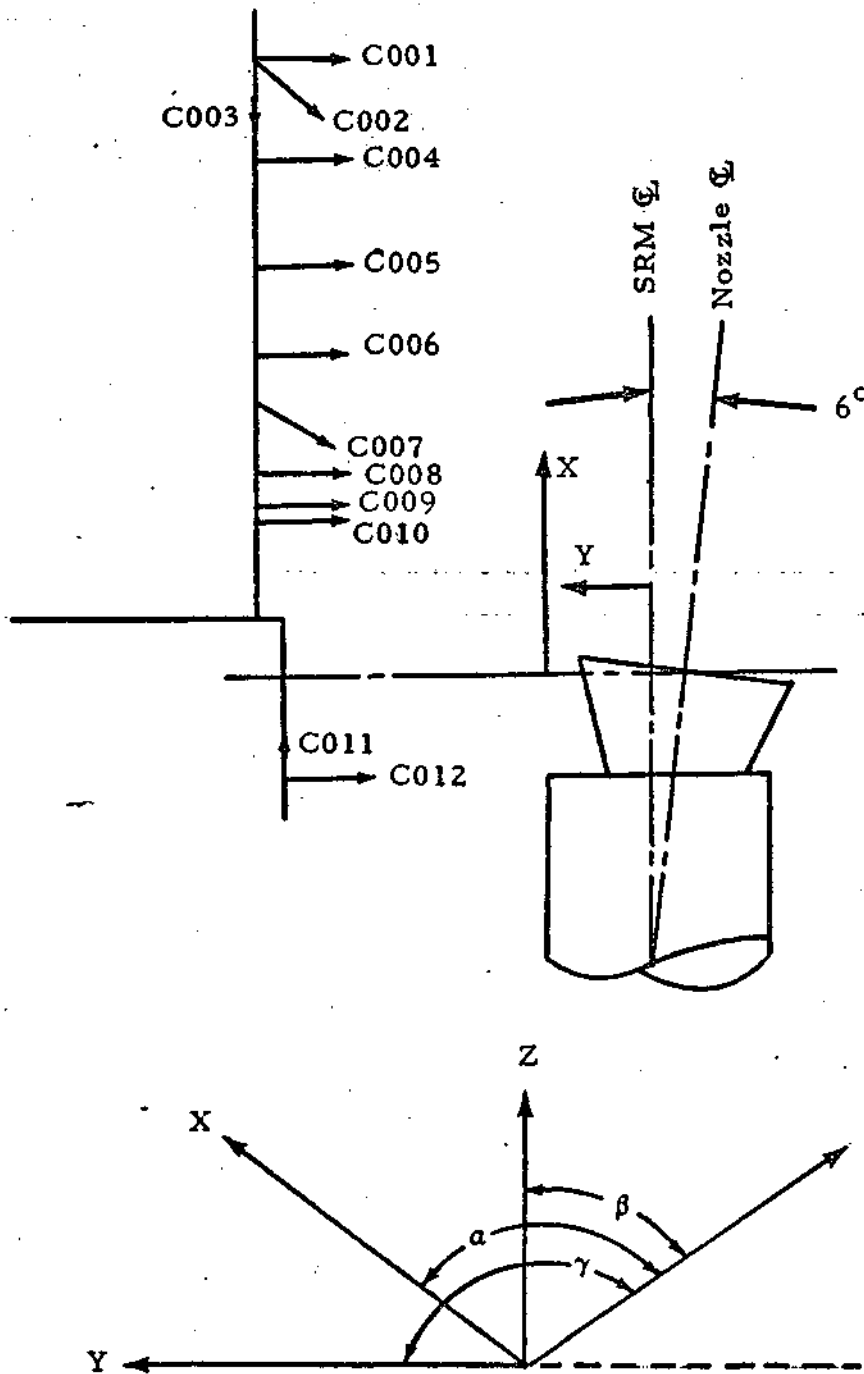
Fig. 3-16 - Calorimeter Locations and Coordinate System

Table 3-1

RADIATION HEAT TRANSFER RATE PREDICTED
BY EACH CALORIMETER

Sensor No.	q min $\left(\dfrac{Btu}{ft^2\text{-sec}}\right)$	q max $\left(\dfrac{Btu}{ft^2\text{-sec}}\right)$	q ave $\left(\dfrac{Btu}{ft^2\text{-sec}}\right)$	q ave/F_v $\left(\dfrac{Btu}{ft^2\text{-sec}}\right)$
C001	11.7	12.5	12.0	22.5
C002	10.7	11.6	11.1	40.1
C003	5.0	5.4	5.2	50.9
C004	11.5	12.1	11.7	23.3
C005	11.8	12.7	12.2	26.6
C006	10.5	11.3	10.8	26.4
C007	5.0	6.0	5.2	21.4
C008	8.6	10.4	9.0	25.8
C009	8.7	9.5	9.1	28.5
C010	0.9	1.9	1.2	48.8
C011	2.1	2.3	2.2	13.3
C012	2.7	3.6	3.3	32.9
C013	0.7	0.8	0.7	11.4
C014	—	—	—	—
C015	—	—	—	—

3-27

Section 4

COMPARISONS OF FLOW FIELDS GENERATED USING A GASEOUS
METHOD-OF-CHARACTERISTICS PROGRAM AND A COUPLED
TWO-PHASE FLOWFIELD PROGRAM

One of the objectives of this contract is to determine how well the present
liquid rocket flowfield analysis programs predict the plume environments of
solid rocket motors (SRMs). The Titan III 120-inch SRM was chosen for this
analysis. Two flowfield computer programs were used to analyze this motor.
These programs are Lockheed's Method-of-Characteristics program (Ref. 2-5)
(liquid or gaseous) and Kliegel's Two-Phase solid rocket motor analysis program
(Ref. 2-2). For the purpose of comparing the results of these two programs,
the nozzle exit plane Mach number and static pressure distributions were
chosen.

Using Lockheed's Method-of-Characteristics program, three different
analyses of the Titan 120-inch SRM were performed. The first two analyses
consisted of running the nozzle using equilibrium chemistry thermodynamic
data generated by the NASA-Lewis CEC program (Ref. 2-6) and ideal gas prop-
erties obtained at the chamber conditions of the equilibrium chemistry. The
third run was made using ideal gas chamber conditions with the specific heat
rates modified to take into account the presence of solid particles. The method
used for modifying the specific heat ratio used here was obtained assuming no
velocity and temperature lags between the gas and the particles, a gas gamma
of 1.15 and a particle to gas mass flow rate ratio of 0.372. This method is
described by Hoffman in Ref. 3-3.

A fourth run was made using Kliegel's coupled two-phase nozzle program
(Ref. 3-2). Kliegel's program is an ideal gas program. The gaseous thermo-
chemistry data used in this run was the same as the ideal gas MOC runs with
a gas gamma of 1.15. The particle to gas loading was 0.372.

4-1

The results of the four runs are presented in Figs. 4-1 and 4-2. Figure 4-1 presents the exit plane distributions of static pressure. The gaseous method-of-characteristics run which matches the Kliegel's two-phase analysis is the run which was made using the modified specific heat ratio. The worst comparison is the equilibrium gaseous MOC analysis. Figure 4-2 presents the exit plane Mach number distributions from the four runs. The Mach number associated with the specific heat ratio MOC run is a gas Mach number modified in a similar fashion to the specific heat. The equations used are also presented in Ref. 3-3.

The results of this study indicate that the best comparisons between gaseous analysis and a two-phase analysis are made using the modified specific heat ratio. The worst comparison is between the equilibrium chemistry gaseous run and the two-phase run. In this case the differences are due to both the two-phase losses and the differences between equilibrium chemistry and ideal gas assumptions. It will be very desirable to make this same comparison between programs when Lockheed's coupled two-phase program described in Section 2 becomes operational with equilibrium chemistry.
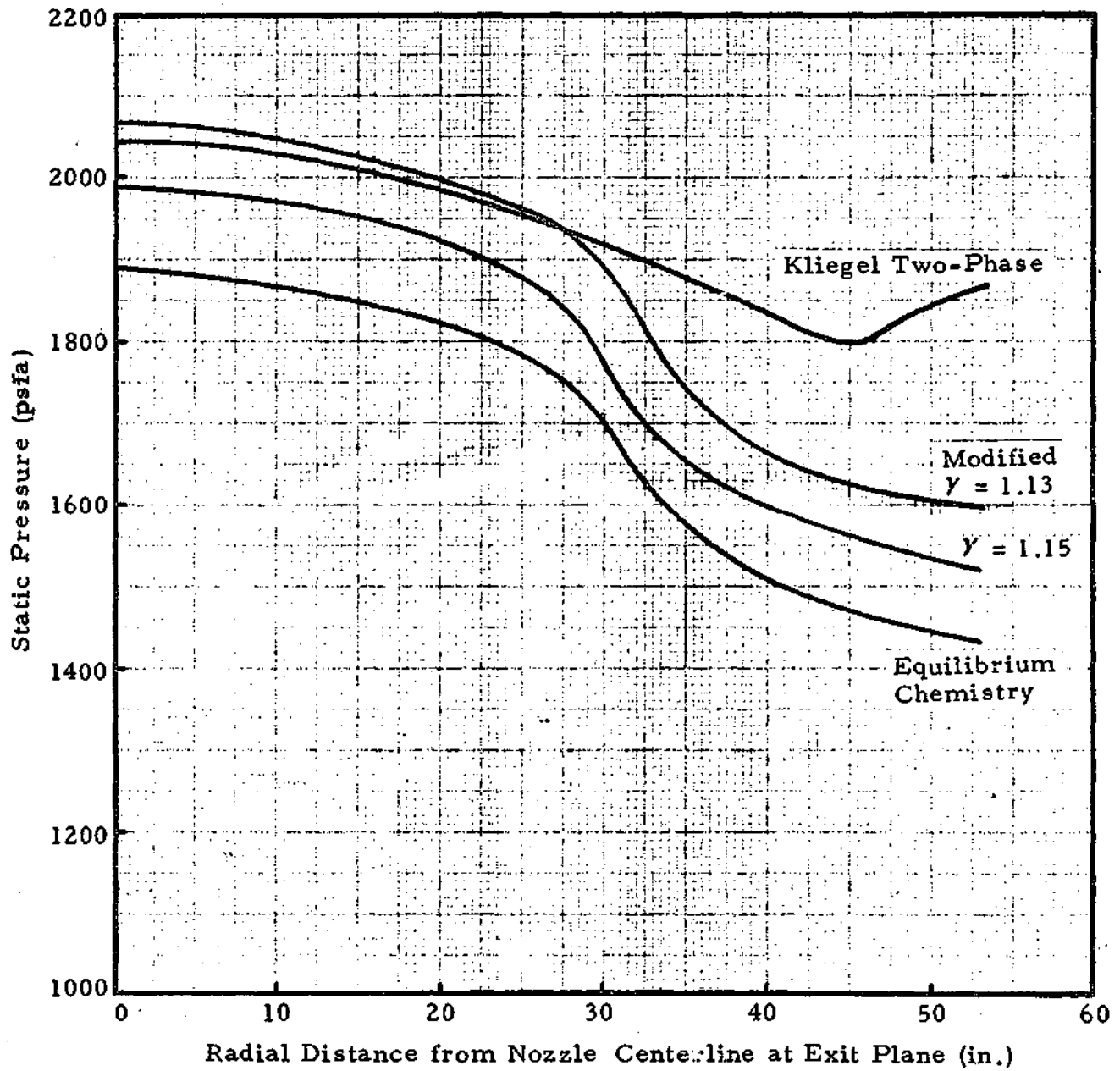
Fig. 4-1 - Exit Plane Static Pressure Distributions for 120-Inch
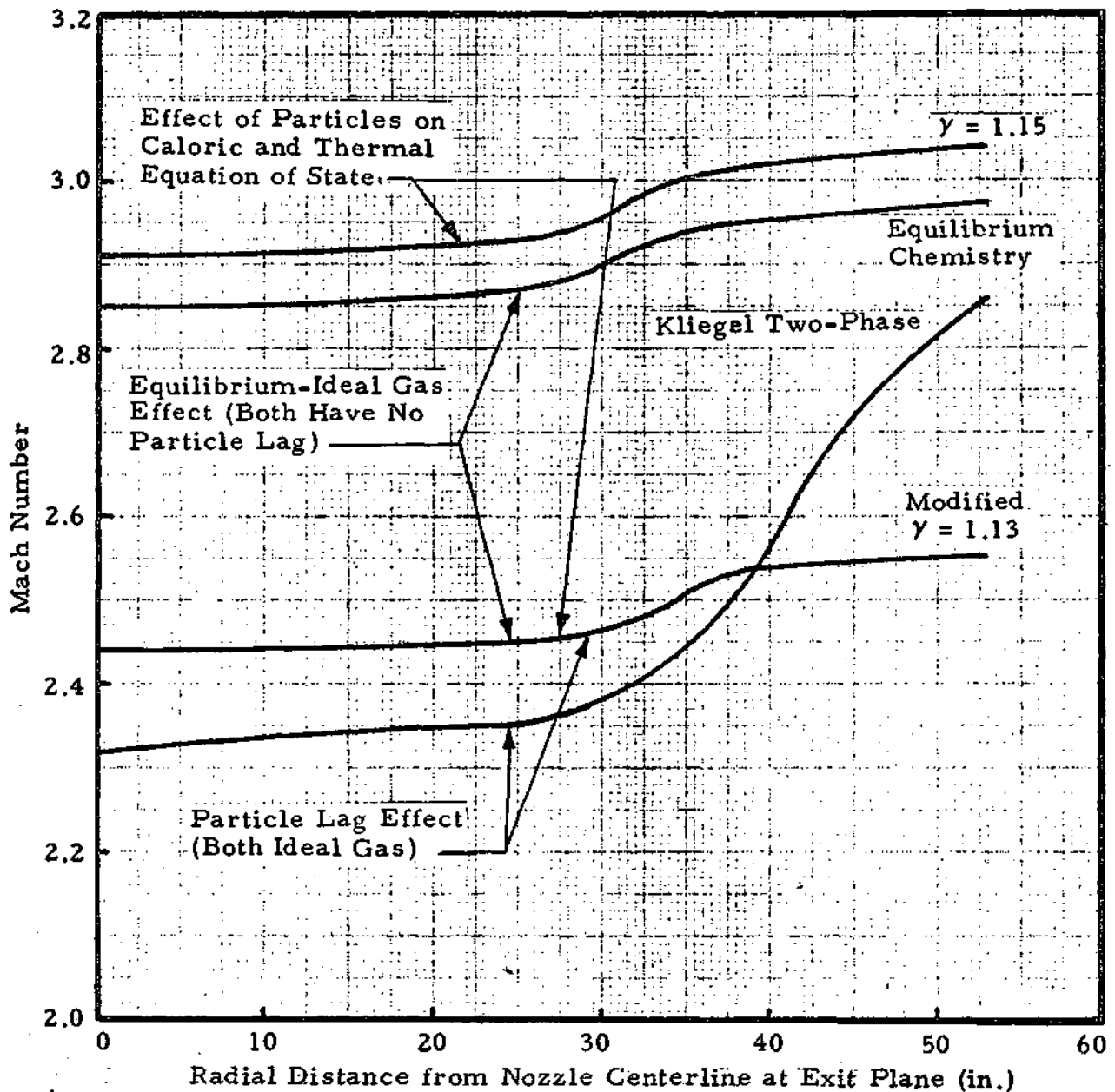Titan III Solid Rocket Motor

4-3

Fig. 4-2 - Exit Plane Mach Number Distributions for 120-Inch Titan III Solid Rocket Motor

Section 5

PLUME IMPINGEMENT OUTFLOW HEATING CORRECTION

Most current theories used in predicting convective heat transfer rates on shuttle-type geometries subjected to exhaust plume impingement do not utilize an adequate outflow correction theory. When a plume impinges on a surface at some angle of inclination, there is an outflow-induced thinning of the boundary layer. If current methods for predicting convective heat transfer without outflow correction theory are used, the predicted heating rates could be considerably lower than the experimentally measured heating rates. In many instances when sufficient experimental data are available, it is very difficult to make experimental-theoretical comparisons. Without outflow analysis to determine the severity of the thinning of the boundary layer and the corresponding increase in convective heating rates, erroneous experimental-theoretical comparisons may result. Convective heating rates determined by turbulent theory may compare more favorably with experimental data than laminar theory. This may lead to an assumption that the experimental data are turbulent which may in actuality be laminar data. When the outflow correction theory is applied the laminar theory should match the laminar data and the turbulent theory should match the corresponding turbulent data.

The purpose of this study is to develop an outflow correction theory that will be used at a future date to modify the existing convective heat transfer methods on the Lockheed-Huntsville Plume Impingement Computer Program (PLIMP) (Ref. 1-1).

5.1 THREE-DIMENSIONAL SURFACE FIT FOR PRESSURE DISTRIBUTIONS

The calculation of inviscid surface streamlines and heating rates are dependent on the surface pressure distribution. Regardless of whether the pressure distribution is determined by experimental or theoretical methods,

it must possess a certain characteristic. The pressure distribution must be such that it can be described by functional means. The function or functions used to describe the pressure distribution must also meet certain requirements in that when differentiated they must yield continuous first and second derivatives in both the axial and circumferential directions. If the pressure distribution could be described by a discrete analytical function, this requirement could be easily met. Unfortunately, however, this is not the case. In general, most if not all, pressure distributions cannot be described by an analytical expression, therefore a numerical technique must be used. The numerical method which seems to best fulfill the requirements is the Method of the Bicubic Piecewise Polynominal Functions. The cubic piecewise polynominal functions of one variable will be discussed first since their results are used to generate the bicubic polynominal functions. The theoretical pressure distributions used in this analysis were obtained from the Lockheed-Huntsville PLIMP program.

5.2   CUBIC PIECEWISE POLYNOMIAL FUNCTIONS

For functions of one variable, such as the cubic piecewise polynomial function, defines a function $P(\phi)$ which assumes values $P_j = P(\phi)_j$ at a given point ϕ_j and matches the derivatives $(dP/d\phi)_j$ at each ϕ_j. See Fig. 5-1.
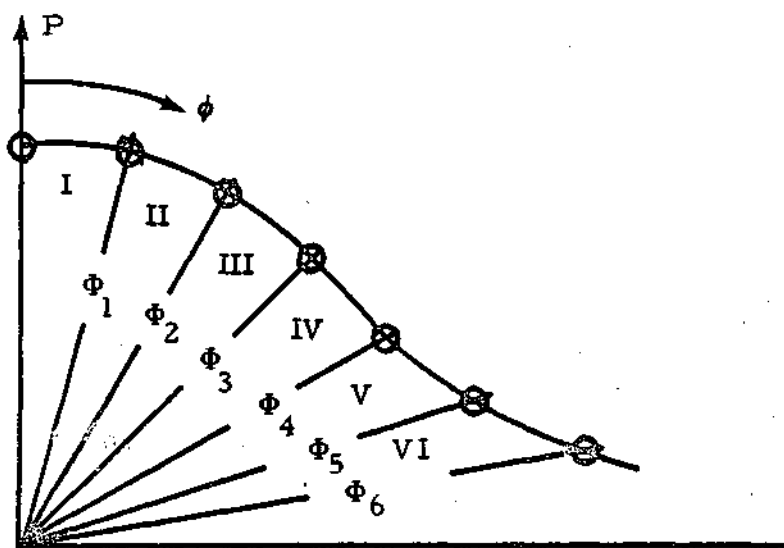

Fig. 5-1 - Cubic Piecewise Polynomial Function of One Variable

Consider the following cubic polynomial

$$P_j(\phi) = C_1 + C_2 \phi_j + C_3 \phi_j^2 + C_4 \phi_j^3 \qquad (5.1)$$

In order to determine the coefficients C_1 - C_4 for the ploynomial $P_j(\phi)$ such that when differentiated it will yield continuous first derivatives, a set of four simultaneous equations must be solved. Three of the four equations are of the form of Eq. (5.1) while the fourth equation is the derivative equation and is of the form of Eq. (5.2)

$$\left(\frac{\partial P}{\partial \phi}\right)_j = C_2 + 2C_3\phi_j + 3C_4\phi_j^2 \qquad (5.2)$$

$$\left(\frac{\partial P}{\partial \phi}\right)_1 = \frac{P_2 - P_1}{\phi_2 - \phi_1} \qquad (5.3)$$

By knowing the function values $P_j(\phi)$ at ϕ_j where $j = 1, 2$ and 3 and the derivative $\left(\frac{\partial P}{\partial \phi}\right)_j$ where $j = 1$ (calculated by Eq. (5.3), a set of four equations can be solved simultaneously for the coefficients C_1 - C_4. These coefficients will be used to compute any pressure or pressure-theta derivative in region I (see Fig. 5-1). The procedure for computing the coefficients for region I is repeated to determine the set of coefficients in each region for regions II through IV. The derivative $\left(\frac{\partial P}{\partial \phi}\right)_j$ where $j = 2$, can now be calculated using the coefficients for region I and Eq. (5.2). Equation (5.1) where $j = 2, 3, 4$ and the derivative $\left(\frac{\partial P}{\partial \phi}\right)_2$ make up a new set of equations which can be solved simultaneously for the coefficients in Region II. The end result is a set of coefficients in each region which when used in Eqs. (5.4) and (5.5) completely

specify the pressure and pressure derivative at any point (ϕ).

$$P(\phi) = C_1 + C_2 \phi + C_3 \phi^2 + C_4 \phi^3 \qquad (5.4)$$

$$\frac{\partial P}{\partial \phi} = C_2 + 2C_3 \phi + 3C_4 \phi^2 \qquad (5.5)$$

The same procedure as has been previously discussed is used to determine the pressure and pressure derivatives in the x direction at constant ϕ values. The cubic piecewise functions have been used to determine the pressure derivatives, $\frac{dP}{d\phi}$ and $\frac{dP}{dx}$, which are continuous derivatives at each grid intersection on Fig. 23. By knowing the pressure and the pressure derivatives with respect to x and y the mixed derivative may be determined by using the following equation

$$\frac{\partial^2 P}{\partial x \partial y} = \frac{1}{2} \cdot \frac{\frac{\partial P}{\partial x}(j+1) - \frac{\partial P}{\partial x}(j)}{\Delta y} + \frac{\frac{\partial P}{\partial \phi}(i+1) - \frac{\partial P}{\partial \phi}(i)}{\Delta y}$$

The bicubic piecewise polynomial functions which describe the pressure surface in each region ($R_{11} - R_{ij}$) can now be determined by knowing the pressure (P) and three derivatives ($\frac{\partial P}{\partial x}$, $\frac{\partial P}{\partial \phi}$, $\frac{\partial^2 P}{\partial x \partial \phi}$) at each grid intersection shown in Fig. 5-2.

5.3 BICUBIC PIECEWISE POLYNOMIAL FUNCTIONS

Consider the following bicubic polynomial.

$$P(x, \phi) = C_{00} + C_{10}x + C_{01}\phi + \ldots C_{33}x^3\phi^3 \qquad (5.7)$$

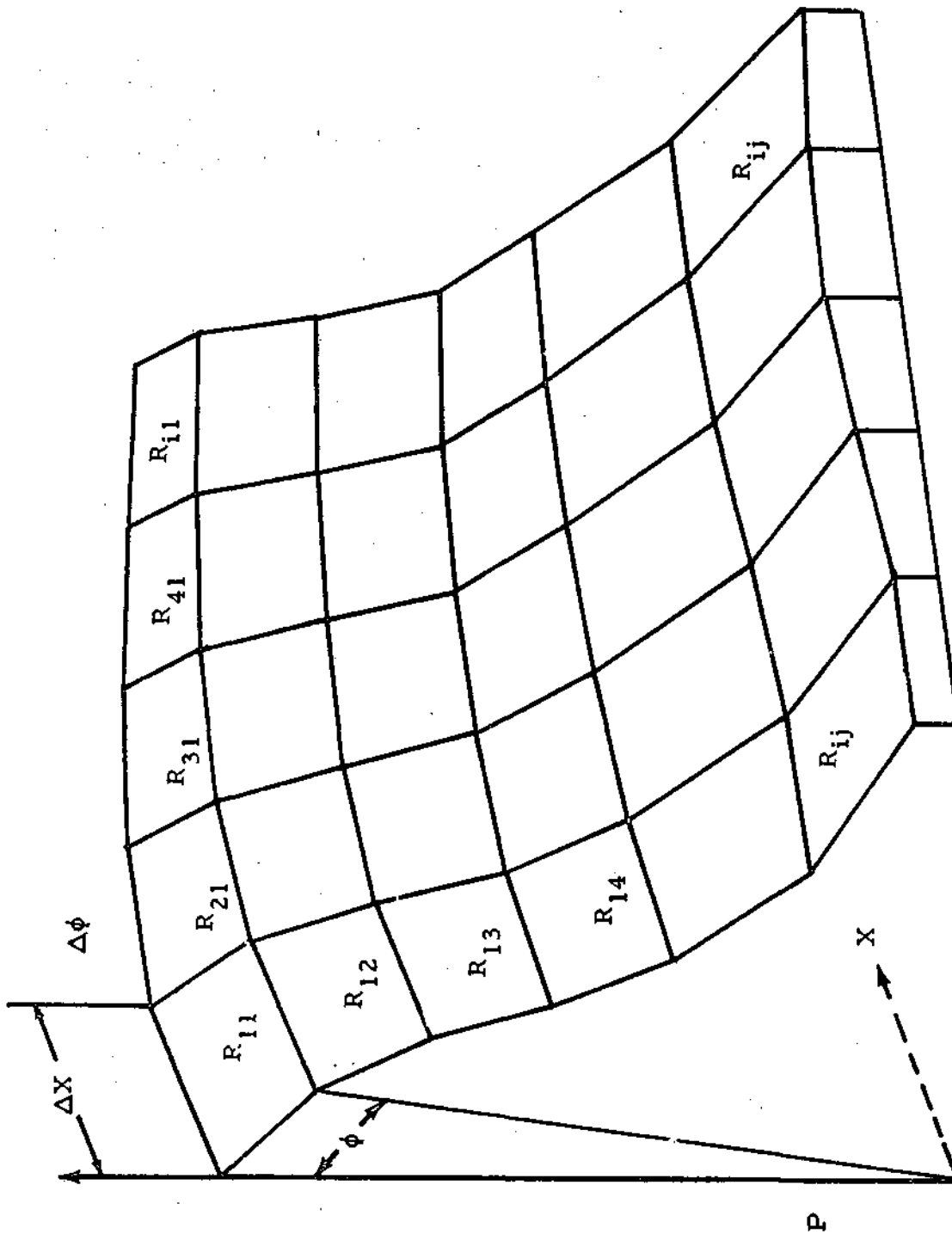$$= \sum_{i=0}^{3} \sum_{j=0}^{3} C_{ij} x^i \phi^j$$

5-4

Fig. 5-2 - Rectangular Grid for Pressure vs X and ϕ

Examining the grid generated in Section 5.2 (Fig. 5-2) a statement can be made that applies in general to all bicubic polynomials. In each R_{ij} there is one and only one bicubic polynomial (Eq. 5-7) which takes on specific values of P, $\frac{\partial P}{\partial x}$, $\frac{\partial P}{\partial \phi}$, $\frac{\partial 2P}{\partial x \partial \phi}$ at the four corners of the grid sections. This means that if these four quantities are specified at each of the four corners, of the grid section of interest, the bicubic polynomial function obtained will be unique to that grid section. When Eq. (5.7) is differentiated it will yield continuous first and second derivatives with respect to x and ϕ at any point within the grid section.

In each grid section, P is a bicubic polynomial (Eq. 5.7). Partial differentation of Eq. (5.7) with respect to ϕ yields,

$$\frac{\partial P}{\partial \phi} (x, \phi) = \sum_{i=0}^{3} \sum_{j=1}^{3} j\, C_{ij}\, x^i \phi^{j-1} \tag{5.8}$$

with respect to x yields

$$\frac{\partial P}{\partial x} (x, \phi) = \sum_{i=1}^{3} \sum_{j=0}^{3} i\, C_{ij}\, x^{i-1} \phi^{j} \tag{5.9}$$

and with respect to x and y yields

$$\frac{\partial^2 P}{\partial x \partial y} (x, \phi) = \sum_{i=1}^{3} \sum_{j=1}^{3} ij\, C_{ij}\, x^{i-1} \phi^{j-1} \tag{5.10}$$

The second pressure derivatives with respect to x and with respect to y are present in Eqs. (5.11) and (5.12).

$$\frac{\partial^2 P}{\partial \phi^2} (x, \phi) = \sum_{i=0} \sum_{j=2} j(j-1) C_{ij} x^i \phi^{j-2} \tag{5.11}$$

$$\frac{\partial^2 P}{\partial x^2} (x, \phi) = \sum_{i=2} \sum_{j=0} i(i-1) C_{ij} x^{i-2} \phi^j \tag{5.12}$$

Each of Eqs. (5.7) through (5.10) is evaluated at each of four corners of the grid section of interest. These equations make up the set of 16 simultaneous equations to be solved for the 16 coefficients describing the surface in the particular grid section.

To achieve a smooth continuous surface fit, as has been previously discussed, continuity in differentiation is a requirement. This quality of the surface fit is obtained by derivative matching (Eqs. (5.8) through (5.10)) at the interface between two successive grid sections as shown on Fig. 5-2. For example, let us examine regions R_{11} and R_{12} in Fig. 5-2. Suppose the coefficients to be used in Eq. (5.7) to describe the surface over Region R_{11} have been calculated. When these coefficients are used in Eqs. (5.8) through (5.10), the equations must yield values for the $\frac{\partial P}{\partial \phi}$, $\frac{\partial P}{\partial x}$ and the $\frac{\partial^2 P}{\partial x \partial y}$ at the intersections between R_{11} and R_{12} that are identical to those previously calculated by the methods in Section 5.1. Likewise, the coefficients calculated for region R_{12} when used in Eqs. (5.8) through (5.10) must yield derivatives which are also identical to those previously calculated at the interface between R_{11} and R_{12}. With this derivative matching continuous first, second, and mixed derivatives are assured. The end results obtained from the bicubic piecewise polynomial functions are presented in Fig. 5-3. The pressure surface is completely
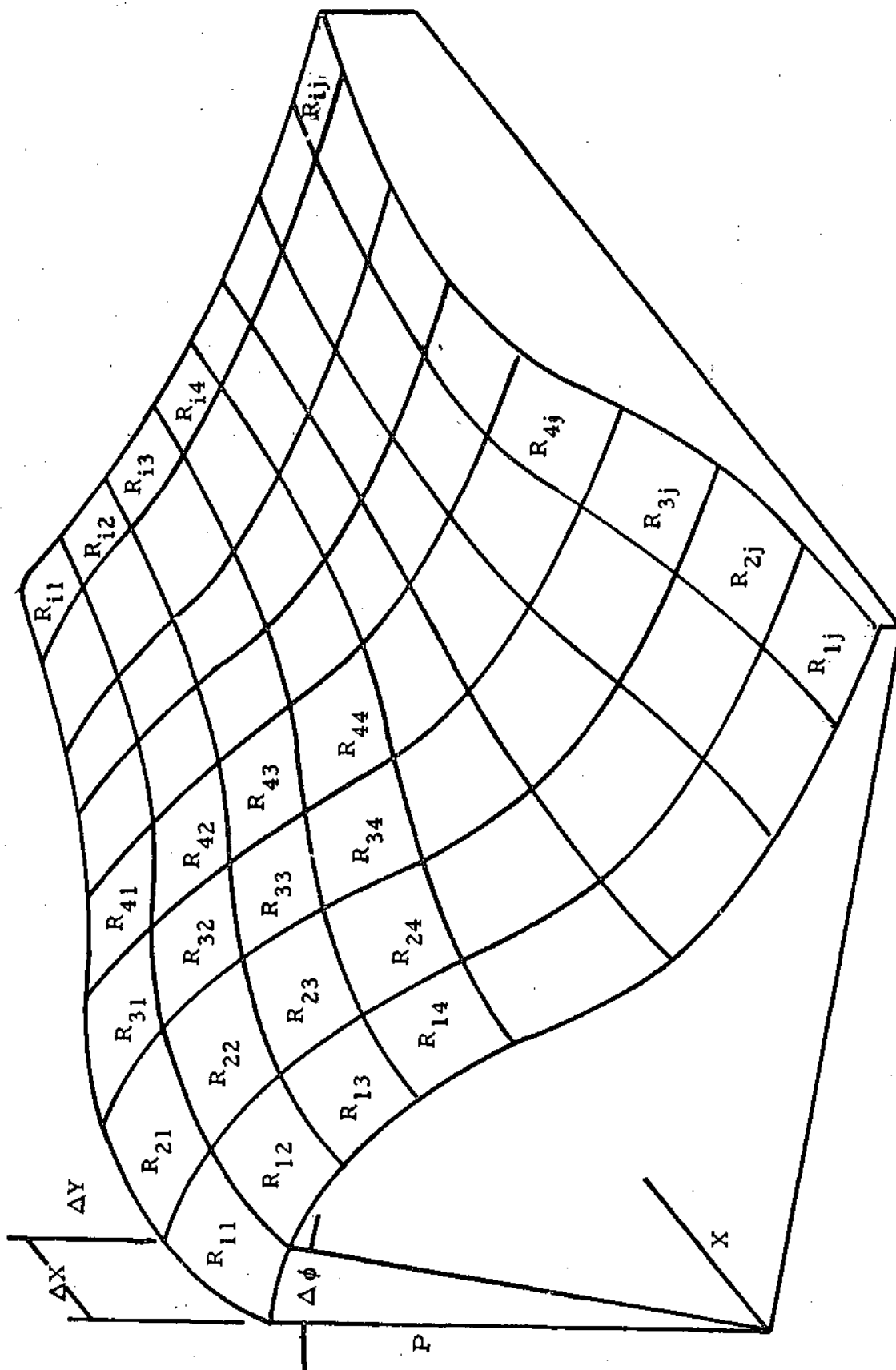
Fig. 5-3 — Smooth Pressure Surface Fit Generated by the Method of the Piecewise Bicubic Polynomial Functions

specified by individual sets of coefficients which uniquely describe a bicubic polynomial function in each region over the entire pressure surface. At any point on the surface, the pressure and pressure derivatives can be determined by using Eqs. (5.7) through (5.12) and the corresponding set of coefficients.

5.4 CROSSFLOW EFFECTS BY STREAMLINE DIVERGENCE THEORY

DeJarnette (Ref. 5-1) has performed extensive studies in the area of streamline divergence theory and its applications to convective heat transfer on reentry vehicles. His methods for determining inviscid surface streamlines on these reentry vehicles will be adapted to problem area of determining the streamline patterns for particular shuttle type geometries subjected to exhaust plume impingement.

To trace an inviscid surface streamline, an orthogonal coordinate system along the streamline must be determined. The geometry of the body is usually represented in a cylindrical coordinate system as $r = f(x, \phi)$ with unit vectors $\hat{e}_x$, $\hat{e}_r$ and $\hat{e}_\phi$ in the x, r and ϕ directions, respectively. (See Fig. 5-4). Since Euler's inviscid momentum equation (Eq. 5-20) only applies along a streamline, a coordinate system along the streamline which can be readily transformed into the original cylindrical coordinate system must be developed. Figure 5-4 shows the unit vectors in each of the two coordinate systems.

The outer unit vector normal to the surface was determined by Dejarnette to be

$$\hat{e}_N = -\sin\Gamma \, \hat{e}_x + \cos\Gamma \, (\cos\delta_\phi \, \hat{e}_r - \sin\delta_\phi \, \hat{e}_\phi) \tag{5.13}$$

The unit vector perpendicular to the curve of the body but not necessarily normal to the body surface is

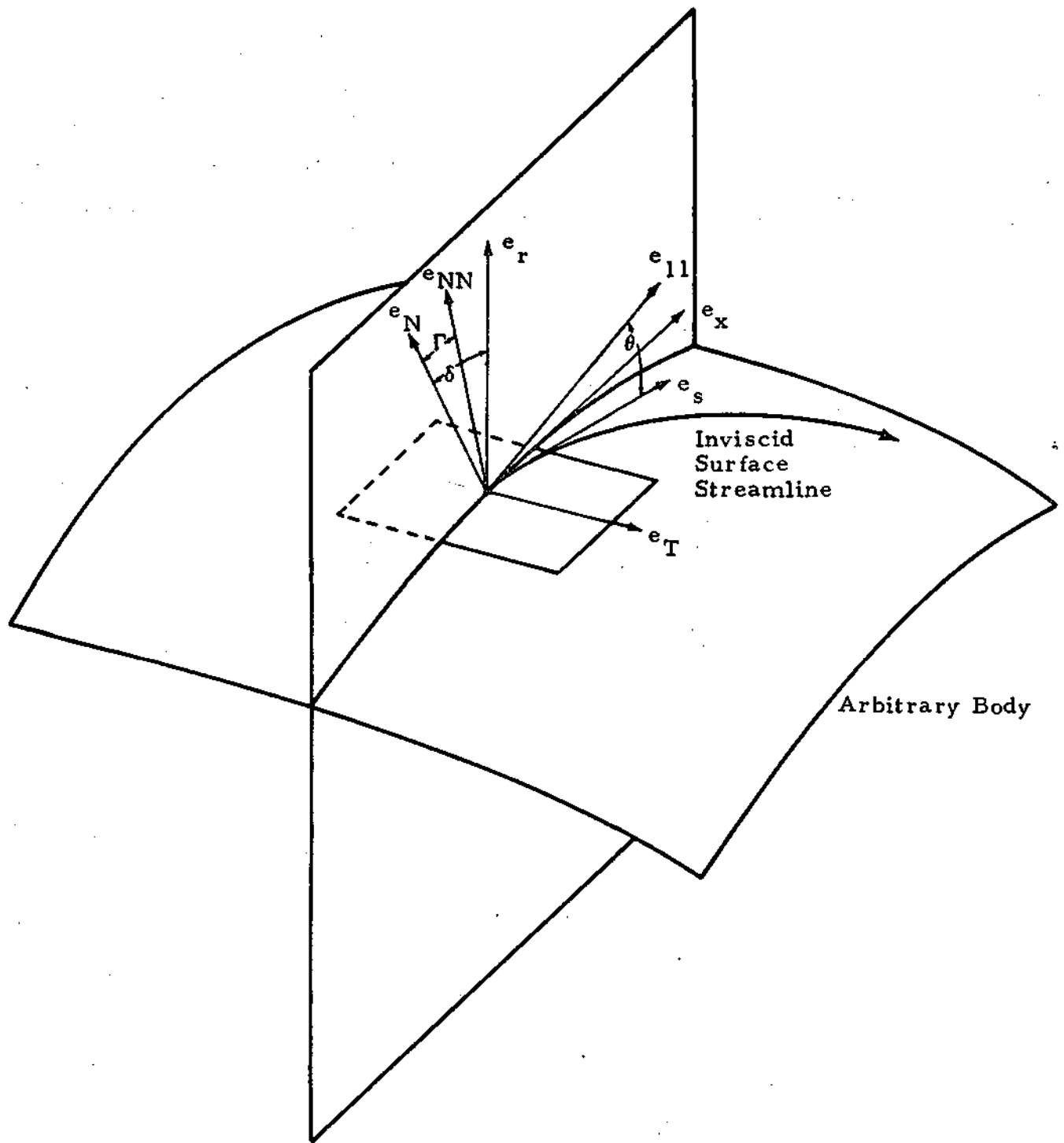$$\hat{e}_{NN} = \cos\delta_\phi \, \hat{e}_r - \sin\delta_\phi \, \hat{e}_\phi \tag{5.14}$$

5-9

Fig. 5-4 - Unit Vector System Used to Determine Streamline Coordinates

By performing the vector cross products (Eqs. (5.14) and (5.15)) the unit vectors $\hat{e}_T$ (a vector tangent to the body surface) and $\hat{e}_{11}$ (a vector tangent to the body surface and perpendicular to the $\hat{e}_T$) can be determined.

$$\hat{e}_T = \hat{e}_x \times \hat{e}_{NN} \tag{5.15}$$

$$\hat{e}_{11} = \hat{e}_N \times \hat{e}_T \tag{5.16}$$

$\hat{e}_s$, a unit vector in the streamline direction can be determined by the following equation.

$$\hat{e}_s = \cos\theta\ \hat{e}_{11} + \sin\theta\ \hat{e}_T \tag{5.17}$$

$\hat{e}_B$ defines a unit vector perpendicular to $\hat{e}_s$ and tangent to the body surface i.e.,

$$\hat{e}_\beta = \hat{e}_s \times \hat{e}_N \tag{5.18}$$

Performing the vector products and making the necessary substitutions the streamline coordinates in terms of the cylindrical coordinates can be written as -

$$\hat{e}_s = \cos\theta\ \cos\Gamma\ \hat{e}_x + (\sin\theta\ \sin\delta_\phi + \cos\theta\ \cos\delta_\phi\ \sin\Gamma)\ \hat{e}_r$$
$$+ (\sin\theta\ \cos\delta_\phi - \cos\theta\ \sin\delta_\phi\ \sin\Gamma)\ \hat{e}_\phi \tag{5.19}$$

$$\hat{e}_\beta = -\sin\theta\ \cos\Gamma\ \hat{e}_x + (\cos\theta\ \sin\delta_\phi - \sin\Gamma\ \sin\theta\ \cos\delta_\phi)\ \hat{e}_r$$
$$+ (\cos\theta\ \cos\delta_\phi + \sin\theta\ \sin\delta_\phi\ \sin\Gamma)\ \hat{e}_\phi \tag{5.20}$$

5-11

5.5 METHOD FOR DETERMINING THE STREAMLINE DIRECTION (θ)

Euler's inviscid momentum equation for determining the angle θ (Fig. 25) along the streamline is

$$\frac{D\vec{V}}{DT} = V \frac{D\vec{V}}{DS} = \frac{-\overline{V}P}{\rho} \tag{5.21}$$

But $\vec{V} = V \hat{e}_s$, therefore Eq. (5.20) becomes

$$\frac{D\vec{V}}{DT} = V \frac{DV}{DS} \hat{e}_s + V^2 \frac{D \hat{e}_s}{DS} = \frac{-\overline{V}P}{\rho} \tag{5.22}$$

In using Euler's equations, it is assumed that there is a constant entropy level on the body surface.

Equation (5.21), expressed in streamline coordinates, becomes

$$\frac{D\theta}{DS} + \sin\Gamma \frac{D\sigma}{DS} = - \frac{1}{\rho V^2} \frac{1}{h} \frac{\partial P}{\partial \beta} \tag{5.23}$$

where h is the metric coefficient that will be discussed later in the report.

DeJarnette, in his analysis, determine the transfomation operators relating the streamline coordinate system to the cylindrical coordinate system (Eqs. (5.24) and (5.25)).

$$\frac{1}{h} \frac{\partial}{\partial \beta} = \frac{1}{h} \frac{\partial x}{\partial \beta} \frac{\partial}{\partial x} + \frac{1}{h} \frac{\partial \phi}{\partial \xi} \frac{\partial}{\partial \phi}$$

$$. = \hat{e}_x \cdot \hat{e}_\beta \ \frac{\partial}{\partial x} + \frac{\hat{e}_\phi \cdot \hat{e}_\beta}{f} \ \frac{\partial}{\partial \phi}$$

$$= - \sin\theta \ \cos\Gamma \frac{\partial}{\partial x} + \frac{(\cos\theta \ \cos\delta_\phi + \sin\theta \ \sin\delta_\phi \ \sin\Gamma)}{f} \ \frac{\partial}{\partial \phi} \qquad (5.24)$$

and

$$\frac{D}{DS} = \frac{1}{h_s} \ \frac{\partial}{\partial \xi} = \frac{1}{h_s} \ \frac{\partial x}{\partial \xi} \ \frac{\partial}{\partial x} + \frac{1}{h_s} \ \frac{\partial \phi}{\partial \xi} \ \frac{\partial}{\partial \phi}$$

$$= \hat{e}_x \cdot \hat{e}_s \ \frac{\partial}{\partial x} + \frac{\hat{e}_\phi \cdot \hat{e}_s}{f} \ \frac{\partial}{\partial \phi}$$

$$= \cos\theta \ \cos\Gamma \frac{\partial}{\partial x} + \frac{(\sin\theta \ \cos\delta_\phi - \cos\theta \ \sin\delta_\phi \ \sin\Gamma)}{f} \ \frac{\partial}{\partial \phi} \qquad (5.25)$$

Using the transformation operators (Eqs. (5.24) and (5.25)), Eq. (5.23) can be expressed in cylindrical coordinates in the following manner.

$$\frac{D\theta}{DS} = - \left(\frac{P_s}{\rho V^2} \right) \left[- \sin\theta \ \cos\Gamma \frac{\partial}{\partial x} \left(\frac{P}{P_s} \right) \right.$$

$$\left. + \frac{(\cos\theta \ \cos\delta_\phi + \sin\theta \ \sin\delta_\phi \ \sin\Gamma)}{f} \ \frac{\partial}{\partial \phi} \left(\frac{P}{P_s} \right) \right]$$

$$- \sin\Gamma \left[\cos\theta \ \cos\Gamma \ \frac{\partial \sigma}{\partial x} + \frac{(\sin\theta \ \cos\delta_\phi - \cos\theta \ \sin\delta_\phi \ \sin\Gamma)}{f} \ \frac{\partial \sigma}{\partial \phi} \right] \qquad (5.26)$$

Also using Eqs. (5.24) and (5.25), the geometric location derivatives with respect to streamline direction were determined to be

$$\frac{Dx}{DS} = \cos\theta \, \cos\Gamma \qquad (5.27)$$

$$\frac{D\phi}{DS} = \frac{\sin\theta \, \cos\delta_\phi - \cos\theta \, \sin\delta_\phi \, \sin\Gamma}{f} \qquad (5.28)$$

For a cylinder, which is the geometry under consideration in this anslysis, the angles Γ and δ_ϕ are identically equal to zero reducing Eqs. (5.26) through (5.28) to

$$\frac{D\theta}{DS} = \left(\frac{P_s}{V^2}\right) \left[-\sin\theta \, \frac{\partial}{\partial x}(P/P_s) + \frac{\cos\theta}{f} \, \frac{\partial}{\partial \phi}(P/P_s) \right] \qquad (5.29)$$

$$\frac{Dx}{DS} = \cos\theta \qquad (5.30)$$

$$\frac{D\phi}{DS} = \frac{\sin\theta}{f} \qquad (5.31)$$

Equation (5.29) can be solved by numerical integration, once the pressure derivatives $\dfrac{\partial(P/P_s)}{\partial x}$ and $\dfrac{\partial(P/P_s)}{\partial \phi}$ are determined. These derivatives are deter-mined by differentiating the piecewise bicubic polynomial functions describing the surface pressure distribution on the cylinder at the correct geometric location determined by Eqs. (5.30) and (5.31). Once the initial streamline direc-tion (θ) is assumed, Eqs. (5.30) and (5.31) can be numerically integrated to deter-mine the correct geometric location (X, ϕ) at which the bicubic functions are evaluated for the $\dfrac{\partial(P/P_s)}{\partial x}$ and the $\dfrac{\partial(P/P_s)}{\partial \phi}$, in Eq. (5.29).

5.6 METHOD OF DETERMINING THE METRIC COEFFICIENT, h

Before presenting the methods for computing the metric coefficient, h, perhaps the physical meaning of the metric coefficient should be presented.
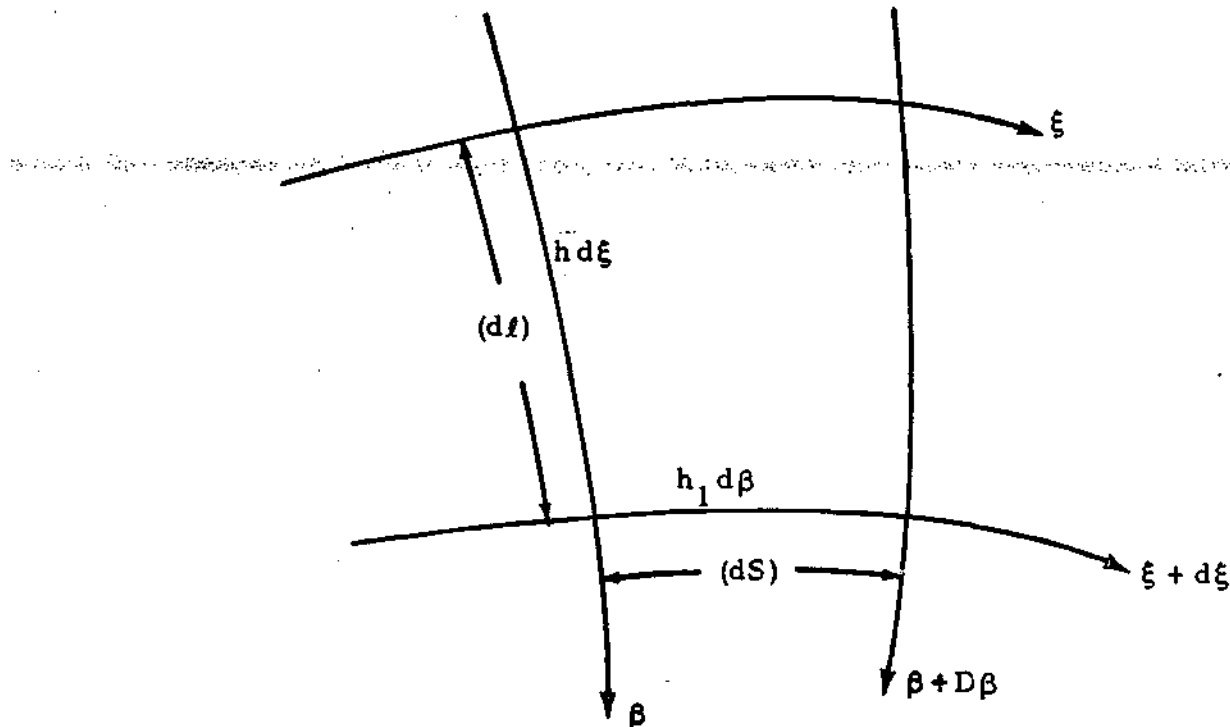

Fig. 5-5 - General Orthogonal Curvilinear Coordinate System

For any general orthogonal curvilinear coordinate, say ξ, β on the surface of a body, the distance between adjacent lines at constant ξ or β will vary from point to point. If increments in these quantities are to be related to actual, physical distances along the surface (dS and dℓ), it is therefore necessary to introduce metric coefficients say h_1 and h_2 such that h, dβ and h_2 dξ are, respectively, small distances (dS and dℓ) measured in the ξ and β directions (see Fig. 5-5). Since the divergence between successive

5-15

streamlines is determine by h, h_1 is not of particular importance. The term h dβ is equal to the integration step size dS for solution of the equations for h.

DeJarnette (Ref. 5-1) suggests the following differential equation for the metric coefficient, h,

$$\frac{Dh}{DS} = \frac{\partial\theta}{\partial\beta} + \sin\Gamma \frac{\partial\sigma}{\partial\beta} \tag{5.32}$$

Using the various substitutions presented in Ref. 5-1, Eq. (5-31) can be expressed as follows to eliminate $\frac{\partial\theta}{\partial\beta}$,

$$\frac{1}{h}\frac{D^2h}{DS^2} = -\left[\frac{P_s}{\rho_s V_\infty^2} \frac{\rho_s}{\rho} \frac{V_\infty^2}{V^2} \frac{1}{h}\frac{\partial}{\partial\beta}(P/P_s)\right]^2 (3 - M^2)$$

$$+ \frac{P_s}{\rho_s V_\infty^2} \frac{\rho_s}{\rho} \frac{V_\infty^2}{V^2} \frac{1}{h}\frac{\partial}{\partial\beta}\left[\frac{1}{h}\frac{\partial}{\partial\beta}(P/P_s)\right]$$

$$+ \frac{\cos^2\Gamma \cos\delta_\phi}{f}\left[\frac{\partial\Gamma}{\partial x}\frac{\partial\sigma}{\partial\phi} - \frac{\partial\sigma}{\partial x}\frac{\partial\Gamma}{\partial\phi}\right] \tag{5.33}$$

Equation (5.32) is a generalized equation which applies to any geometry. Reducing this equation for a cylinder yields

$$\frac{1}{h}\frac{D^2 h}{DS^2} = -\left[\frac{P_s}{\rho V^2}\left(-\sin\theta\ \frac{\partial P}{\partial x} + \frac{\cos\theta}{f}\ \frac{\partial P}{\partial \phi}\right)\right]^2 (3 - m^2)$$

$$- (\frac{1}{h}\frac{Dh}{Ds})\left(\frac{P_s}{\rho V^2}\right)\left(\cos\theta\ \frac{\partial P}{\partial x} - \frac{\sin\theta}{f}\ \frac{\partial P}{\partial \phi}\right)$$

$$+ \frac{P_s}{\rho V^2}\left(\frac{1}{f}\ \sin\theta\ \cos\theta\ \frac{\partial P}{\partial \phi} + \sin^2\theta\ \frac{\partial^2 P}{\partial x^2}\right.$$

$$\left. - 2/f\ \sin\theta\ \cos\theta\ \frac{\partial^2 \rho}{\partial x \partial \phi} + \frac{\cos^2\theta}{f^2}\ \frac{\partial^2 P}{\partial \phi}\right) \qquad (5.34)$$

The derivatives, $\frac{\partial P}{\partial x}$, $\frac{\partial P}{\partial \phi}$, $\frac{\partial^2 P}{\partial x^2}$, $\frac{\partial^2 P}{\partial \phi^2}$, and the $\frac{\partial^2 P}{\partial x\ \partial \phi}$ are determined from the surface pressure fit. This equation along with Eqs. (5.29) through (5.31) are solved simultaneously by a numerical integration routine (Runge-Kutta) for the geometric location of the streamline (x, ϕ), the streamline angle (θ) and the metric coefficient, H.

5.7 RELATIONSHIP OF THE METRIC COEFFICIENTS TO CONVECTIVE HEAT TRANSFER THEORY

5.7.1 Laminar Convective Heat Transfer

Heat transfer through a laminar boundary layer is calculated using the integral form of the energy equation. The effects of variable freestream properties (velocity, density and pressure) are accounted for through use of the appropriate transforms of the flat plate solution. Non-constant properties through the boundary layer are also accounted for.

The effects of variable gas properties through the boundary layer on laminar boundary layer heat transfer are determined by evaluating the gas properties at a "reference enthalpy" and using these values in the constant

property solutions obtained by Blasius. Based on this method, the convective heat transfer rate to the wall is evaluated using

$$q = g_h (H_r - h_w) \tag{5.35}$$

where the adiabatic wall or recovery enthalpy is

$$H_r = \int_o^{T_e} C_p \, dT + \frac{r V_e^2}{2 Jg} \tag{5.36}$$

where

$$r = \sqrt{Pr} \tag{5.37}$$

The enthalpy conductance g_h is evaluated from the Stanton number (St)

$$St = \frac{g_h}{\rho^* V_e} = \frac{Nu^*}{Re^* Pr^*} \tag{5.38}$$

The "reference enthalpy" h^* can be determined by

$$h^* = h_e + 0.5 (H_s - h_e) + 0.22 (H_r - h_e) \tag{5.39}$$

The Blasius flat plate solution assuming constant property flow is

$$\frac{Nu}{\sqrt{Re}} = 0.332 \, Pr^{1/3} \tag{5.40}$$

5-18

By making the necessary subsitutions and noting that

$$Re^* = \frac{\rho^* V_e X_L}{\mu^*} \tag{5.41}$$

Equation (5.34) becomes

$$\dot{q} = \frac{0.332}{Pr^{*2/3}} \frac{(\rho^* \mu^* V_e)^{0.5}}{X_L^{.5}} (H_r - h_w) \tag{5.42}$$

The term X_L in Eq. (5.42) is the characteristic running length and can be obtained by numerically integrating the following equation along a flowfield streamline

$$X_L = \frac{1}{\rho^* \mu^* V_e h^2} \int_0^S \rho^* \mu^* V_e h^2 \, dS \tag{5.43}$$

where S is the distance along the streamline and h is the metric coefficient.

5.7.2 Turbulent Convective Heat Transfer

The equation for turbulent convection heat transfer is

$$\dot{q} = \frac{0.0296}{Pr^{*0.66}} (\rho^* V_e)^{0.8} \left(\frac{\mu^*}{XT}\right)^{.2} (H_r - h_w) \tag{5.44}$$

where X_T is the turbulent characteristic running length and can be calculated by Eq. (5.45)

$$X_T = \frac{1}{\rho^* \mu^* V_e h^{1.25}} \int_0^S \rho^* \mu^* V_e h^{1.25} \, dS \tag{5.45}$$

5-19

Again, as in the laminar case, the metric coefficients contributions to the characteristic running length are revealed.

5.8   RESULTS

A digital computer program using the theory presented in the preceding section was developed to calculate inviscid surface streamlines on a cylinder subjected to exhaust plume impingement. The pressure distribution used by the program was calculated by the Lockheed-Huntsville PLIMP program (Ref. 2-3) and is presented graphically in Fig. 5-6. Figure 5-7 is a plot of the inviscid streamline coordinates (ϕ versus x) for several initial streamline starting angles, θ, while Fig. 5-8 is a plot of the metric coefficient versus distance X for one of these streamlines ($\theta = 0.10$). Notice in Fig. 5-7 how the streamlines diverge at an increasing rate as they proceed axially down the cylinder. This divergence, i.e., the spreading of the streamlines, is reflected by the metric coefficient plot in Fig. 5-8. The metric coefficient increases at a moderate rate to X = 4 inches. From X = 4 inches to X = 4.5 inches, there is a sudden abrupt increase in the metric coefficient that can be attributed to the increased spreading between streamlines.
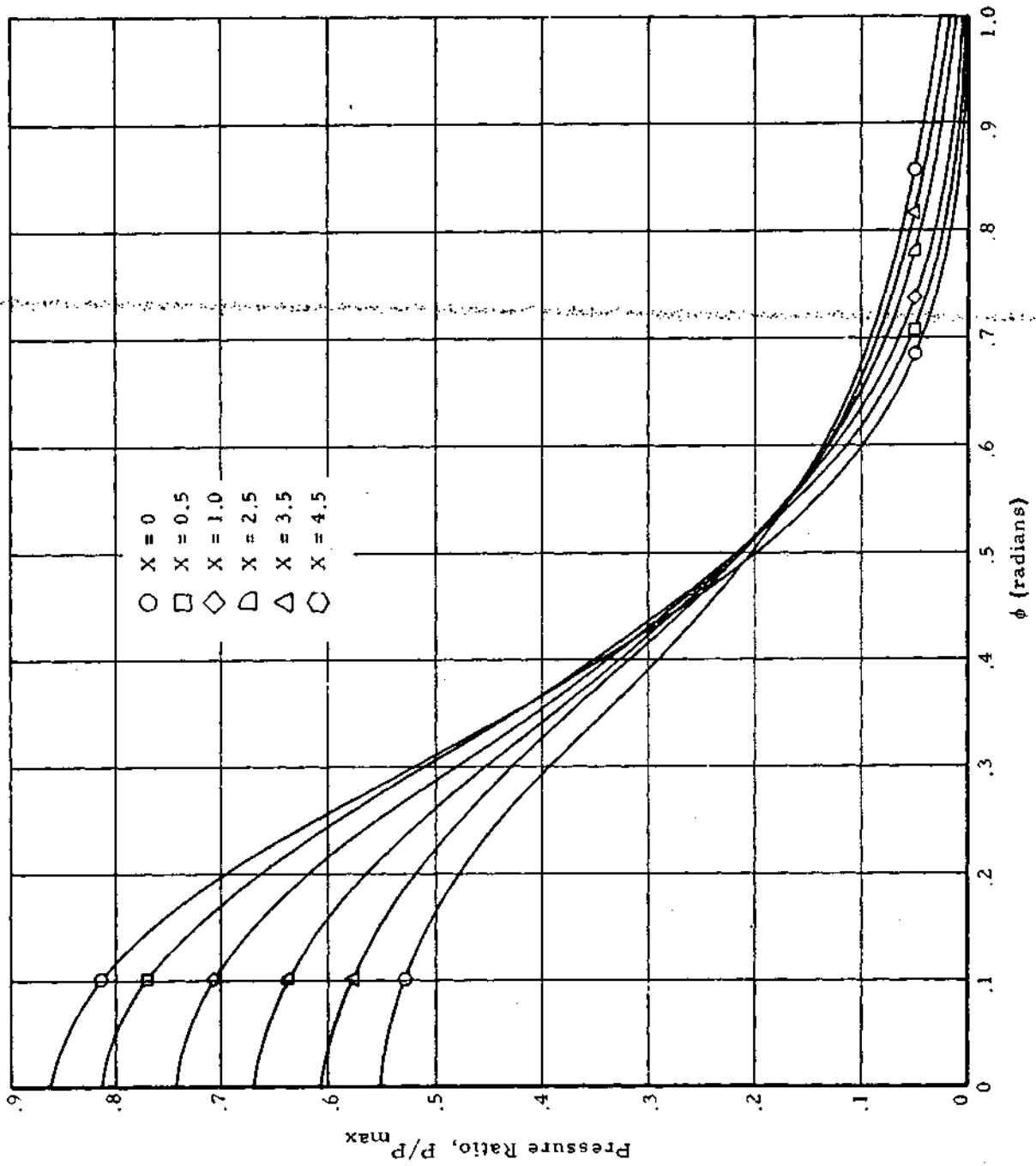
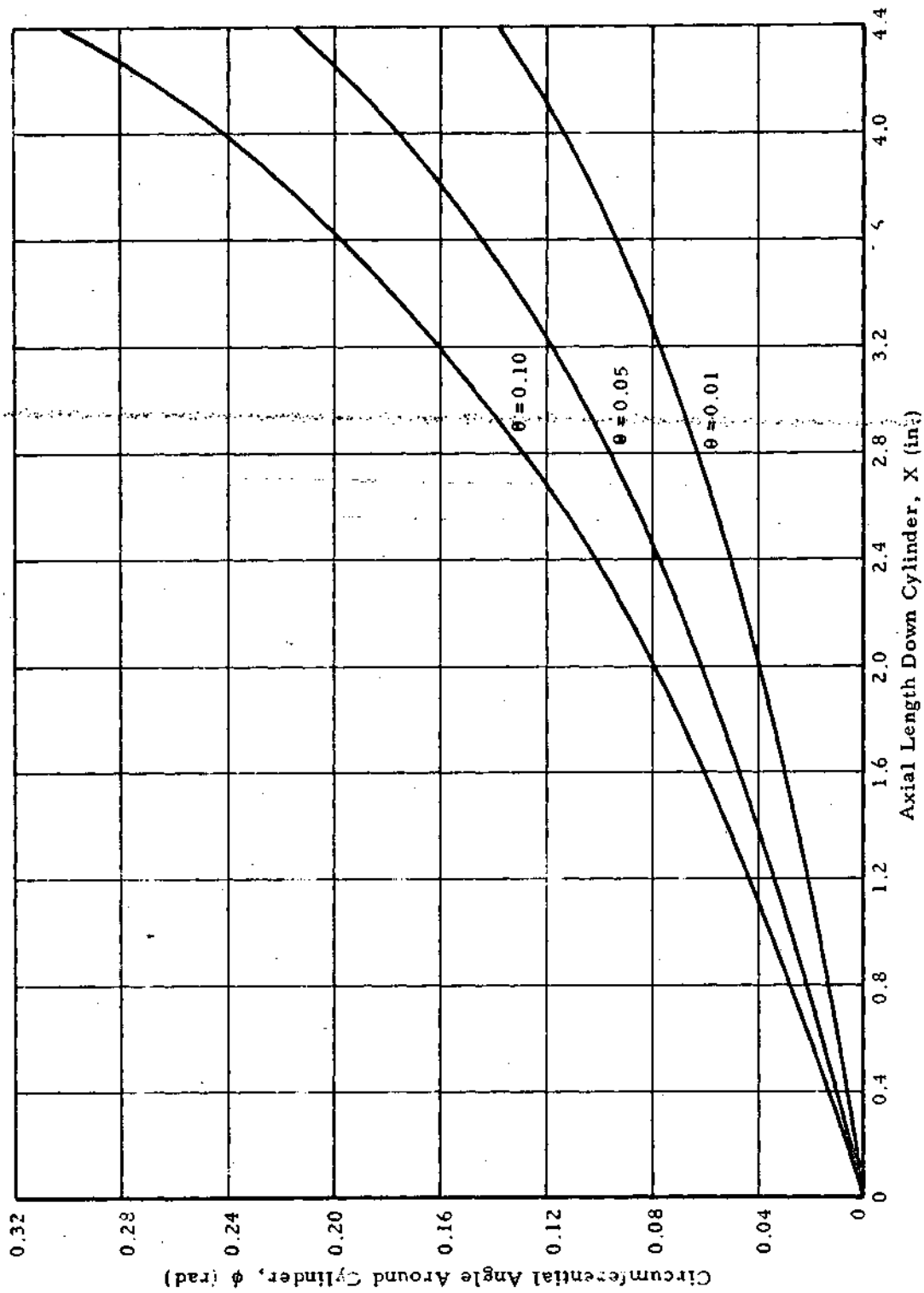Fig. 5-6 - Surface Pressure Distribution for a Cylinder

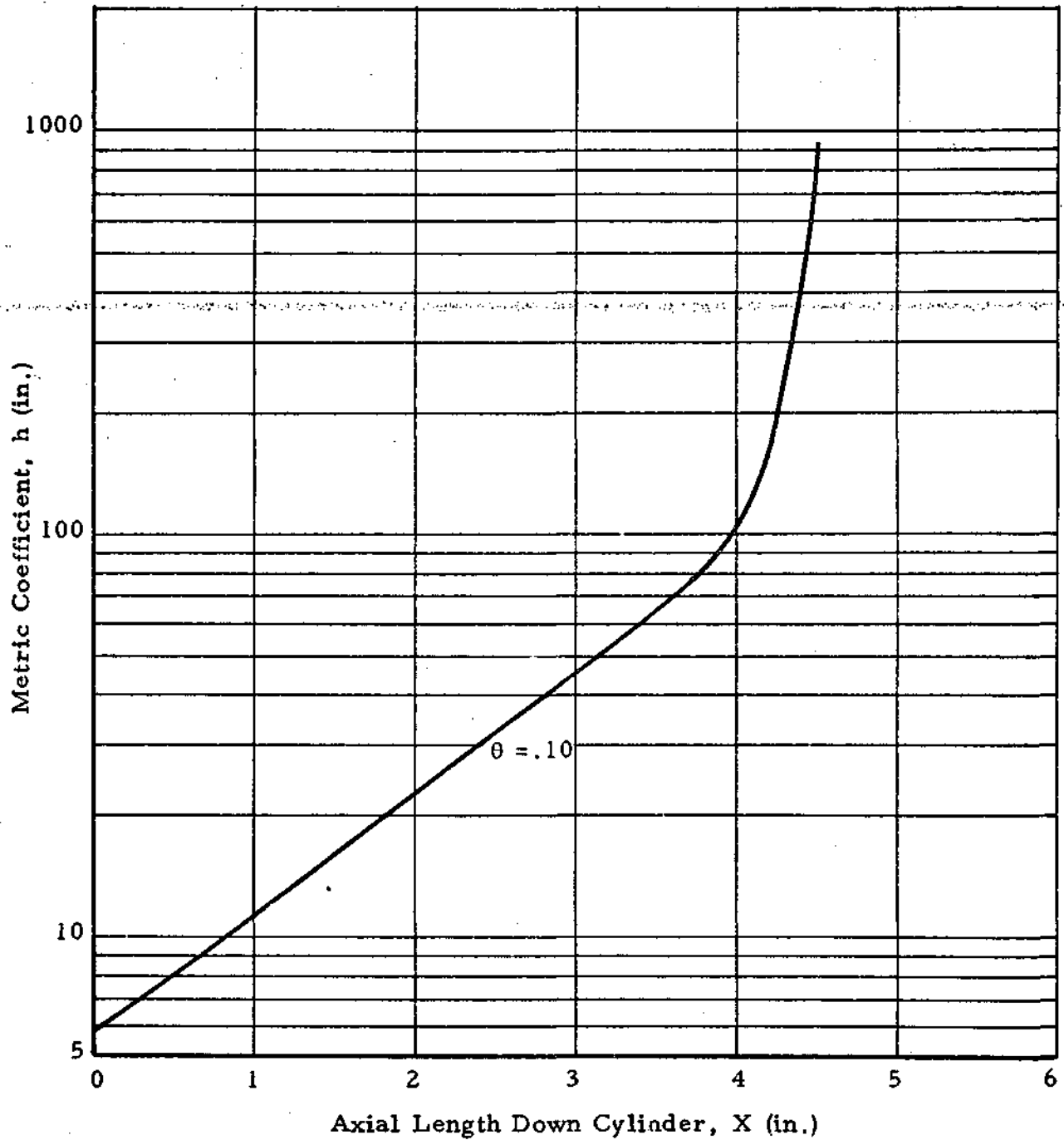Fig. 5-7 - Streamline Coordinates Plot for Various Initial Starting Angles, θ

Fig. 5-8 - Metric Coefficient vs Axial Length Down Cylinder

Section 6
CONCLUSIONS

Development of an equilibrium coupled two-phase computer program for solid rocket motor nozzle and plume analysis has been initiated and described. This program will provide a description of the exhaust of solid rocket motors which may be utilized in performing base heating and plume impingement analysis for the space shuttle vehicle. A comparison of techniques for predicting solid motor exhaust flowfields was presented which indicates significant differences in the predicted flow fields obtained using a two-phase computer program and a gaseous flowfield program.

A plume impingement convective heat transfer theory with outflow corrections was presented that could be incorporated into the heat transfer portion of the Plume Impingement program which would result in an outflow corrected heat transfer analysis which may be important for shuttle-type vehicle applications.

The solid particle radiation analysis for the Titan 120-inch motor and simulated shuttle motor presented in this report is based on several quantities including: the particle environment, particle size distribution, the scattering and absorption coefficients of the particles, the index of refraction of the particles as a function of temperature and wave length and the radiance of the particle cloud. The technique used in this analysis has shown that better data on scattering and absorption coefficients and index of refraction of the alumina particles is desirable for any future analysis of shuttle motors. Also a technique for more easily obtaining radiation data once more than one line of sight should be considered. With the development of the equilibrium coupled two-phase analysis a more reliable flow field for obtaining radiation heat transfer data will be realized.

6-1

Section 7
REFERENCES

1-1. Penny, Morris M., and Carl J. Wojciechowski, "User's Manual and Description of a Computer Program for Calculating Heating Rates, Forces and Moments Acting on Bodies Immersed in Rocket Exhaust Plumes," LMSC-HREC D162867-II, Lockheed Missiles & Space Company, Huntsville, Ala., March 1971.

2-1. Laderman, A.J., et al., "Study of Thermal Radiation, Particle Impingement Heating and Flowfield Analysis of Solid Propellant Rocket Exhausts," WO 2386, Philco-Ford-Aeronutronic Division, Newport Beach, Calif., April 1967.

2-2. Kliegel, J.R., and G.R. Nickerson, "The Calculation of Supersonic Gas-Particle Flows in Axisymmetric Nozzles by the Method of Characteristics," STL 6120-8345-TU000, Space Technology Laboratories, Inc., Los Angeles, 1 May 1962.

2-3. Penny, M.M., "Development of a Multiple Shock Computer Program Using a Streamline-Normal Technique," LMSC-HREC A791268-II, Lockheed Missiles & Space Company, Huntsville, Ala., April 1968.

2-4. Ruo, S.R., "Development of a Multiple Shock Computer Program Using a Streamline-Normal Technique," LMSC-HREC A791047, Lockheed Missiles & Space Company, Huntsville, Ala., January 1968.

2-5. Smith, S.D., and A.W. Ratliff, "User's Manual-Variable O/F Ratio Method of Characteristics Program for Nozzle and Plume Analysis," LMSC-HREC D162220-IV, Lockheed Missiles & Space Company, Huntsville, Ala., June 1971.

2-6. Gordon, Sanford, and Bonnie J. McBride, "Computer Program for Calculation of Complex Chemical Equilibrium Compositions, Rocket Performance, Incident and Reflected Shocks and Chapman-Jouguet Detonations," NASA SP-273, NASA-Lewis Research Center, Cleveland, Ohio, 1971.

3-1. Will, C.F., "Thermal Environment Computer Program for Solid Rocket Exhaust Analysis," TN AP-69-419, Chrysler, New Orleans, La., June 1970.

3-2. Kramer, O.G., "Evaluation of Thermal Radiation from the Titan III Solid Rocket Motor Exhaust Plumes," AIAA 5th Thermophysics Conference, Los Angeles, Calif., No. 70-842, July 1970.

3-3. Hoffman, J.D., "An Analysis of the Effects of Gas-Particle Mixtures on the Performance of Rocket Nozzles," TM 63-1, Jet Propulsion Center, Purdue University, Lafayette, Indiana, January 1963.

5-1. PeJarnette, F.R., "Calculation of Inviscid Surface Streamlines and Heat Transfer on Shuttle-Type Configurations," NASA CR 11921, Langley Research Center, Hampton, Va., August 1971.